Condensed Matter Science

Micro/Nanostructure

Experimental assessment of strain gradient plasticity theories
Barney, M.M., G.H. Campbell, J.S. Stölken, W.E. King, R.O. Ritchie

Hard tissue ablation and modification with IR lasers
Fried, D., T. Breunig

High resolution study of the thermomechanical behavior of Al(0.5wt% Cu) thin films by scanning x-ray microdiffraction (µSXRD)
Tamura, N., B.C. Valek, R. Spolenak, R.S. Celestre, A.A. MacDowell, H.A. Padmore, B.W. Batterman, J.R. Patel

In-situ synchrotron x-ray microdiffraction study of deformation behavior in copper-polycrystals during uniaxial deformations
Joo, H.D., J.S. Kim, K.H. Kim, N. Tamura, Y.M. Koo

Lateral inhomogeneities and termination in ultrathin block copolymer films
Fink, R., Th. Schmidt, N. Rehse, G. Krausch, I. Koprinarov, H. Ade

Magnetic switching by spin injection
Stamm, C., S. Andrews, A. Scholl, C.T. Rettner, J.-U. Thiele, J. Stöhr

Microstructure and pinning properties of hexagonal-disc shaped single crystalline MgB_2
Jung, C.U., J.Y. Kim, P. Chowdhury, K.H.P. Kim, S.-I. Lee, N. Tamura, W.A. Caldwell, J.R. Patel

Optimization of PEEM-2 for studies of organic thin film
Morin, C., A.P. Hitchcock, H. Ikeura-Sekiguchi, A. Scholl, A. Doran, K. Kaznacheyev

Polarization-dependent soft-x-ray absorption of highly oriented ZnO microrod-array
Guo, J.-H., L. Vayssieres, C. Persson, R. Ahuja, B. Johansson, J. Nordgren

Quantum confinement observed in α-Fe_2O_3 nanorod-array
Guo, J.-H., L. Vayssieres, C. Såthe, S.M. Butorin, J. Nordgren.

Recent achievements with magnetic soft x-ray microscopy at XM-1
Fischer, P., D. Goll, T. Eimüller, G. Schütz, G. Bayreuther, T. Ono, G. Denbeaux, W. Bates, E. Anderson

Resonant x-ray fluorescence holography: Three-dimensional atomic imaging in true color
Omori, S., L. Zhao, S. Marchesini, M. A. Van Hove, C. S. Fadley

Soft x-ray absorption spectroscopy of *single* nanocrystals
Nolting, F., J. Rockenberger, J. Lüning, J. Hu, A.P. Alivisatos

Spin-resolved electronic structure studies of ultrathin films of Fe on singular and vicinal GaAs
Spangenberg, M., E.A. Seddon, E.M.M. McCash, T. Shen, S.A. Morton, D. Waddill, J. Tobin

Strain and stress in a thin film $YBa_2Cu_3O_x$ bicrystal grain boundary on $SrTiO_3$ substrate studied by x-ray micro-diffraction
Caldwell, W.A., N. Tamura, R.S. Celestre, A.A. MacDowell, H.A. Padmore, J.R. Patel

X-ray spectromicroscopy of branched polyolefin blends
Appel, G., I. Koprinarov, G.E. Mitchell, A.P. Smith, H. Ade

Experimental assessment of strain gradient plasticity theories

M.M. Barney[1, 2], G.H. Campbell[2], J. S. Stölken[2], W.E. King[2], R.O. Ritchie[1]
[1] Lawrence Berkeley National Laboratory, University of California, Berkeley, California 94720, USA
[2] Lawrence Livermore National Laboratory, University of California, Livermore, California 94551, USA

INTRODUCTION

Classical plasticity theories generally assume that the stress at a point is a function of strain at that point only. However, when gradients in strain become significant, this localization assumption is no longer valid. These conventional models fail to display a 'size effect'. This effect is seen experimentally when the dimension characteristic of the physical phenomenon involved is on the order of the microstructural scale of interest. Under these conditions, strain gradients are of a significant magnitude as compared to the overall strain and must be considered for models to accurately capture observed behavior.

The mechanics community has been actively involved in the development of strain gradient theories for many years. Recently, interest in this area has been rekindled and several new approaches have appeared in the literature. Two different approaches are currently being evaluated. One approach considers strain gradients as internal variables that do not introduce work conjugate higher order stresses. Another approach considers the strain gradients as internal degrees of freedom that requires work conjugate higher order stresses. Experiments are being performed to determine which approach models material behavior accurately with the least amount of complexity. A key difference between the two models considered here is the nature of the assumed boundary conditions at material interfaces. Therefore, we are investigating the deformation behavior of metal/sapphire interfaces loaded under simple shear. To determine the lattice rotations near the boundary, we are examining the samples with submicron X-ray methods and with diffraction techniques in the transmission electron microscope. The experimentally found boundary conditions shall be subsequently used to determine whether the simpler internal variable model is adequately descriptive. This information will also be included in the mesoscale simulations to be carried out as part of the LLNL Multiscale Materials Modeling Project.

BACKGROUND

Although not predicted by classical models, an increase in flow stress is seen during deformation when the observed phenomena is on the order of a micron and inhomogeneties are present. For example, Fleck et.al. [1] showed that when loaded in torsion, a wire displays greater strength for smaller radii. Others authors have observed this type of effect in other systems, including bending [2], indentation hardness [3], and particle hardened alloys [4]. The increase in hardness under these conditions is attributed to the additional dislocations needed for compatibility. These dislocations are commonly referred to as geometrically necessary dislocations [5]. The presence of these dislocations can be ignored and continuum theories applied at large size scales since gradients in strain are small. However, at smaller size scales, more dislocations are formed in a smaller area, resulting in large strain gradients and higher flow stresses. When strain gradients become significant, this localization assumption in continuum theories is no longer valid [6]. This must be accounted for in a non-local theory to accurately reflect material response. Two distinct classes of models that extend classical theories to include strain gradient effects are currently being evaluated. Fleck and Hutchinson [7] have developed one approach (referred to as the FHS model [8]) that considers strain gradients as internal degrees of freedom and requires thermodynamic work conjugate higher order stresses, which need additional boundary conditions. Acharya and Bassani [9] have developed an alternative approach in which a strain gradient term is included in the hardening function. In this method, the strain gradients are considered to be internal variables, which do not introduce higher order stresses or additional boundary conditions. This approach has the advantages that it is simpler overall, preserves the structure of the classical boundary value problem, and can easily be implemented into existing finite element codes. However, the higher order theory may be more predictive because it allows for constraints on strain to be enforced at interfaces. The additional boundary conditions in the higher order theory allow for the presence of a

boundary layer. Specifically, Fleck and Hutchinson [7] determined theoretically that a boundary layer of lattice rotation should be present at an interface between dissimilar materials loaded under remote simple shear. Since boundary layers are not predicted in Acharya and Bassani's approach, detecting the presence of these layers at interfaces will supply critical information in the continued development of strain gradient plasticity theories. Boundary layers seem likely in real materials, since stress fields that are strongly affected by boundaries [10] govern dislocation motion. The presence of a boundary layer, however, has not yet been definitively determined. Although previous experimental work on bicrystals by Sun et.al [11] suggests the presence of a boundary layer, the data are difficult to interpret due to the movement of the grain boundary. Therefore, experiments performed at a metal-ceramic interface are proposed to determine deformation behavior without the complication of grain boundary movement.

EXPERIMENTAL PROCEEDURE

The deformation behavior near an interface is investigated using samples composed of 25μm thick aluminum foils sandwiched between sapphire rods (see [12] for more details). An ultra-high vacuum diffusion-bonding machine [13] is used to bond the two materials. The metal layer is sheared using asymmetric four point bending. This test is used to achieve a uniform simple shear stress state. This stress state is needed to shed light on existing strain gradient models, because each model considered predicts different behavior under this condition. Finite element modeling is used to simulate this experiment in order to confirm the homogeneity of the deformation. The sapphire is modeled as an isotropic elastic material and the metal is modeled as a J_2 linear hardening material. The modeling confirms that the metal layer is under a homogeneous stress state, but does exhibit some edge effects in the strain profiles. This will not affect the experimental results, because observations are only made in the center of the sample.

In order to detect the presence of a boundary layer in the aluminum near the sapphire, the lattice rotations need to be measured from the center of the aluminum layer to an interface in one micron steps. To measure the rotation, the mechanically tested samples were cut into slices for observation of diffraction patterns in a transmission electron microscope (TEM). Unfortunately, standard TEM sample preparation methods cause the aluminum to recrystallize, so a non-destructive method is desired. Unlike most X-ray techniques, the submicron X-ray technique developed at the Advanced Light Source (ALS) [14] uses a small enough spot size to properly investigate the lattice rotation changes in these samples. Unfortunately, the noise from the surface damage layer formed during the polishing of the aluminum is obscuring the signal from the Laue patterns in the bulk region. It has not been possible to fully analyze this data. From some initial analysis, there does appear to be a measurable change in lattice rotation as the interface is approach. However, improved sample preparation techniques to produce a stronger signal need to be employed to confirm this initial indication. Confirming or refuting the presence of this boundary layer is the primary result of the experimental program. If the boundary layer is present, its characterization will be critical in providing parameters for the FHS model. Continued improvement of the model will be facilitated by further experimental results generated by continued investigations. The cyclic feedback of information between experiments and modeling has proven to be successful in other parts of the Multiscale Materials Modeling Project at Lawrence Livermore National Laboratory.

ACKNOWLEDGMENTS

The authors would like to thank Dr. Ralph Spolenak and Dr. Nobumichi Tamura for assistance with the ALS beamline 7.3.3 and for data analysis.

REFERENCES

1. N. A. Fleck, G. M. Muller, M. F. Ashby, and J. W. Hutchinson, Acta Metall. Mater. **42**, 475 (1993).
2. J. S. Stölken and A. G. Evans, Acta. Mater. **46**, 5109 (1998).

3. N. A. Stelmashenko, M. G. Walls, L. M. Brown, and Y. V. Milman, in *Mechanical Properties and Deformation Behavior of Materials Having Ultra-Fine Microstructures*, edited by M. Nastasi, D. M. Parkin, and H. Gleiter. (NATO ASI Series E 233, 1993) pp. 605-610.
4. D. J. Lloyd, Int. Mater. Rev. **39**, 1 (1994).
5. M. F. Ashby, Philos. Mag. **21**, 399 (1970).
6. E. C. Eringen, *Microcontinuum Field Theories* (Springer, New York, 1999).
7. . A. Fleck and J. W. Hutchinson, J. Mech. Phys. Solids **41**, 1825 (1993).
8. J.Y. Shu and N.A. Fleck, J. Mech. Phys. Solids **47**(2), 297 (1999).
9. A. Acharya and J. Bassani, in *Micromechanics of Plasticity and Damage of Multiphase Materials*, IUTAM Symposium, Paris. Aug. 29 - Sept 1, 1995.
10. A. Wikström, Report **261**, Department of Solid Mechanics, Royal Institute of Technology, Stockholm, Sweden, 2000.
11. S. Sun, B.L. Adams, C. Shet, S. Saigal, and W. King, Scripta Met. **39**, 501 (1994).
12. M. M. Barney, G. H. Campbell, J. S. Stölken, J. M. Plitzko, W. E. King, and J.W. Morris, Multiscale Modeling of Materials, Editors: L.P. Kubin, J.L. Bassani, K. Cho, H. Gao, R.L.B. Selinger, MRS Proceedings Volume 653, Materials Research Society, Warrendale, PA, 2001.
13. W. E. King, G.H. Campbell, A.W. Coombs, G.W. Johnson, B.E. Kelly, T.C. Reitz, S.L. Stoner, W.L. Wien, and D.M. Wilson, in *Joining and Adhesion of Advanced Inorganic Materials*, edited by A. H. Carim, D. S. Schwartz and R. S. Silberglitt (Mat. Res. Soc. Symp. Proc. **314**, Pittsburgh, PA, 1993) p. 61.
14. A.A.MacDowell, R.S.Celestre, N.Tamura, R.Spolenak, B.C. Valek, W.L.Brown, J.C.Bravman, H.A.Padmore, B.W.Batterman & J.R.Patel, Nuclear Instruments and Methods in Physics Research A **467-468**, 936 (2001).

This work performed under the auspices of the Division of Materials Science of the Office of Basic Energy Sciences, U.S. Department of Energy, and the University of California Lawrence Livermore National Laboratory under contract No. W-7405-Eng-48.

Principal investigator: Robert O. Ritchie, Ernest Orlando Lawrence Berkeley National Laboratory. Email: roritchie@lbl.gov. Telephone: 510-486-5798.

Hard Tissue Ablation and Modification with IR Lasers

D. Fried and T. Breunig,
Department of Preventive and Restorative Dental Sciences, 707 Parnassus Ave. University of California
San Francisco, 94143-0758

Infrared lasers are ideally suited for the selective and precise removal of carious dental hard tissue while minimizing the healthy tissue loss. Since the initial investigations of Stern[1] over 30 years ago, several unique laser applications have evolved for dentistry, namely laser ablation of dental hard tissue, caries inhibition treatments by localized surface heating, and surface conditioning for bonding[2]. During high intensity laser irradiation, marked chemical and physical changes may be induced in the irradiated dental enamel. These changes can have profound effects on the laser ablation/drilling process and may lead to a reduction in the ablation rate and efficiency, increase peripheral thermal damage and even lead to stalling without further removal of tissue with subsequent laser pulses. Moreover, thermal decomposition of the mineral can lead to changes in the susceptibility of the modified mineral to organic acids in the oral environment. Morphological changes may result in the formation of loosely attached layers of modified enamel that can delaminate leading to failure during the bonding to restorative materials [3, 4]. Therefore, it is important to thoroughly characterize the laser (thermal) induced chemical and crystalline changes after laser irradiation. The mineral, hydroxyapatite, found in bone and teeth contains carbonate inclusions that render it highly susceptible to acid dissolution by organic acids generated from bacteria in dental plaque. Upon heating to temperatures in excess of 400 °C, the mineral decomposes to form a new mineral phase that has increased resistance to acid dissolution[5]. Recent studies suggest that as a side effect of laser ablation, the walls around the periphery of a cavity preparation will be transformed through laser heating into a more acid resistant phase with an enhanced resistance to future decay[6]. However, poorly crystalline non-apatite phases of calcium phosphate may have an opposite effect on plaque acid resistance[7] and may increase the quantity of poorly attached grains associated with delamination failures.IR spectroscopy has been used for half a century to study the structure of bony tissue[8, 9]. Fowler and Kuroda [7, 10] used IR transmission spectroscopy to show the chemical changes induced in laser irradiated dental enamel. Recently, we demonstrated that FTIR in specular reflectance mode could be used effectively to nondestructively measure the laser-induced chemical changes in enamel and that the carbonate loss could be determined as a function of incident laser intensity[11]. However, this technique requires smooth surfaces of large area in order to acquire suitable spectra. The high brightness of the ALS enables spectra to be acquired on specific areas across ablation craters with a resolution of 10 µm.

FTIR spectroscopy was used in the specular reflectance mode for resolving thermally induced changes in dental hard tissue as a result of laser irradiation. High spatial resolution (10 µm) was used with the high brightness available on beam line 1.4.3 for these studies. IR spectra of modified bovine enamel were acquired after laser ablation using several laser wavelengths from the UV to the mid-IR. Specific areas within the laser-ablated region were examined to determine the structural and chemical composition

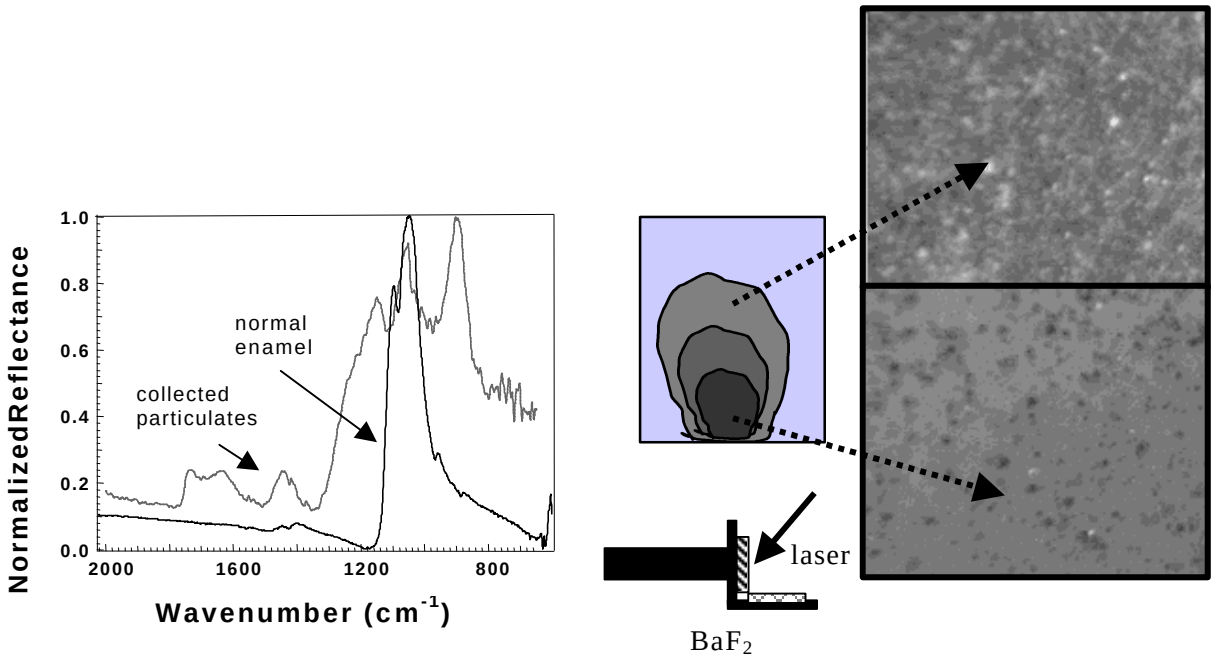

Fig. 1 Spectra of ejected particles collected in vacuum after the laser ablation of enamel using a 9.6 µm TEA CO_2 laser. The particles are deposited in a fan shaped distribution on a BaF_2 substrate. Optical images (320x) of the low density zone (top) and high density zone (bottom) are shown on the right. SR-FTIR spectra of the particles(gray) and normal enamel are shown on the left.

changes associated with the ablation process. The energy deposition and maximum temperature are greatest at the center of crater created by the ablation process and decreases with distance from the crater center. The chemical composition of the crater walls deviated significantly from that of hydroxyapatite after Er:YAG and CO_2 laser irradiation without added water. The high spatial resolution of beam line 1.4.3 allowed identification of the mineral phases present on the crater walls [12, 13] These mineral phases have not been previously reported because of the limited resolution of conventional IR spectroscopy systems.

We postulated that the non-apatite mineral phases originate from the plume of ejected material above the ablated area. In order to confirm that hypothesis, we collected the ablated mineral phases on BaF_2 substrates in vacuum. SR-FTIR spectra were used to show the distribution of phases as a function of distance from the site of laser ablation (Fig. 1). Such data confirms that the mineral phase distribution around the ablation craters is due to recondensation from the plume. We are continuing this effort with other laser wavelengths, energy deposition conditions, and quantities of water to determine the optimum ablation conditions with limited subsurface damage and improved surface conditions for bonding or resistance to environmental degradation. Supported by NIH/NIDCR R29DE12091.

1. Stern R.H.and Sognnaes R.F.: Laser beam effect on hard dental tissues. J. Dent. Res. 43:873, 1964.
2. Wigdor H.A., Walsh J.T., Featherstone J.D.B., Visuri S.R., Fried D.and Waldvogel J.L.: Lasers in Dentistry. Lasers Surg. Med. 16:103-133, 1995.

3. Altshuler G.B., Belikov A.V., Erofeev A.V.and Skrypnik A.V.: Physical aspects of cavity formation of Er-laser radiation, Lasers in Dentistry, Vol. 2394. 211-222 (SPIE, San Jose, 1995).
4. Rechmann P., Glodin D.S.and Hennig T.: Changes in surface morphology of enamel after Er:YAG irradiation, Lasers in Dentistry IV, Vol. 3248. 62-68 (SPIE, San Jose, 1998).
5. Featherstone J.D.B.and Nelson D.G.A.: Laser effects on dental hard tissue. Adv. Dent. Res. 1:21-26, 1987.
6. Konishi N., Fried D., Featherstone J.D.B.and Staninec M.: Inhibition of secondary caries by CO2 laser treatment. Amer. J. Dent. 12:213-216, 1999.
7. Fowler B.and Kuroda S.: Changes in heated and in laser-irradiated human tooth enamel and their probable effects on solubility. Calcif. Tissue Int. 38:197-208, 1986.
8. Constantz P.W.B.a.B.: Hydroxyapatite and Related materials (CRC Press, Boca Raton, 1994).
9. Elliot J.C.: Structure and Chemistry of the Apatites and other Calcium Orthophosphates (Elsevier, Amsterdam, 1994).
10. Kuroda S.and Fowler B.O.: Compositional, structural and phase changes in *in vitro* laser-irradiated human tooth enamel. Ca1cif. Tissue Int. 36:361-369, 1984.
11. Fried D., Murray M.W., Featherstone J.D.B., Akrivou M., Dickenson K.M.and Duhn C.: Dental hard tissue modification and removal using sealed TEA lasers operating at λ=9.6 µm. J. Biomedical Opt. 196-203, 2001.
12. Ashouri N., Shori R., cheung J.M.and Fried D.: IR Laser Ablation of Dental Enamel: Influence of an Applied Water Layer on Ablation Rate and Peripheral Damage, Lasers in Dentistry VII, Vol. 4249, 72-79 (2001).
13. Fried D.and Breunig T.M.: Infrared Spectroscopy of Laser-irradiated Dental Hard Tissues using the Advanced light Source, Lasers in Dentistry VII, Vol. 4249, 99-104 (2001).

Principal investigator: Dan Fried, University of California, San Francisco, 415-502-6641, fried@itsa.ucsf.edu.

High Resolution Study of the Thermomechanical Behavior of Al(0.5wt% Cu) Thin Films by Scanning X-Ray Microdiffraction (μSXRD)

N. Tamura[1], B.C. Valek[3], R. Spolenak[2], R.S. Celestre[1], A.A. MacDowell[1], H.A. Padmore[1], B.W. Batterman[1,4] and J.R. Patel[1,4]

[1]Advanced Light Source, Ernest Orlando Lawrence Berkeley National Laboratory, University of California, Berkeley, California 94720, USA

[2]Agere Systems, formerly Bell Laboratories, Lucent Technologies, Murray Hill NJ 07974

[3]Dept. Materials Science & Engineering, Stanford University, Stanford CA 94305

[4]SSRL/SLAC, Stanford University, P.O. Box 43459, Stanford CA 94309, USA

INTRODUCTION

Materials properties such as strength, resistance to fatigue, and failure ultimately depend on the microstructural features of the material, such as grains, grain boundaries, inclusions, voids and other defects. The so-called mesoscopic length scale (approximately between 0.1 and 10 μm) is receiving increasing attention, both theoretically and experimentally, in order to understand the mechanical behavior of polycrystalline samples as they experienced various constraints. Compared to single crystals, polycrystals are a highly inhomogeneous medium where local stress and structure variations are likely to play an important role in the overall macroscopic behavior of the material. In the present study, we are applying the Scanning X-Ray Microdiffraction (μSXRD) technique developed at the ALS [1,2] to probe local strain/stress and grain orientation in Al(0.5wt% Cu) thin films and compare the results with those obtained with conventional averaging techniques such as wafer curvature.

EXPERIMENTAL

The samples investigated are sputtered Al (0.5 wt.% Cu) thin film test structures originally designed for electromigration studies. The patterned lines, passivated with 0.7 μm of SiO_2 (PETEOS), have dimensions 0.7 or 4.1 μm in width, 30 μm in length and 0.75 μm in thickness. Ti shunt layers are present at the bottom and the top of the lines. A 100 x 100 μm bond pad on the chip with a thin Ti underlayer is used to simulate a bare blanket film.

The samples were scanned under a submicron size white X-ray beam and at each step a white beam Laue diffraction pattern in reflective geometry was collected. The patterns were analyzed in order to yield the orientation and deviatoric strain/stress tensor under each illuminated points of the samples. The outputs of the analysis are grain orientation and strain/stress maps.

The bond pad (blanket film) was thermally cycled between 25°C and 345°C in 40° steps. At each temperature increment, a 15x15 μm area of the film was scanned with the focused white x-ray beam in 1 μm steps. A 0.7 μm wide line and 4.1 μm wide line were scanned in 0.5 μm intervals at room temperature. In addition, a 0.7 μm line was mapped in 0.5 μm steps across the line and 1 μm steps along the line at several temperatures during a cycle between 25°C and 305°C.

RESULTS

A 5x5 μm area preliminary scan of the blanket film shows that while the film is (111) textured within 3°, the deviatoric stresses $\sigma_{xx}' \neq \sigma_{yy}'$ (In the x,y,z orthogonal coordinate system, z is the

out-of-plane direction). In particular, at the granular and subgranular level, the stress can depart significantly from biaxiality. However, if we average the data over the 5 × 5 μm scanned area, biaxiality is retrieved, i.e.: $\langle\sigma'_{xx}\rangle \approx \langle\sigma'_{yy}\rangle$. The average biaxial stress of the film can be computed assuming that the out-of-plane average total stress $\langle\sigma_{zz}\rangle = 0$. Expressing the total average stress matrix as the sum of the deviatoric and hydrostatic stress components one can show that the average biaxial stress $\langle\sigma_b\rangle = \langle\sigma_{xx}\rangle = \langle\sigma_{yy}\rangle = \langle\{(\sigma'_{xx}+\sigma'_{yy})/2\} - \sigma'_{zz}\rangle$.

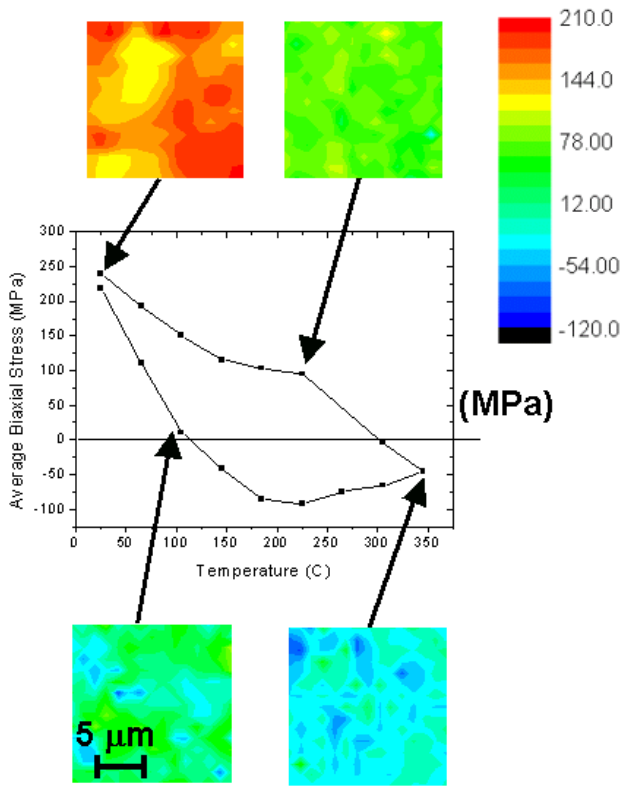

Figure 1. Thermal cycling results on a 15×15 μm area of an Al(Cu) bond pad (blanket film) showing the averaged biaxial stress component $\langle\sigma_b\rangle$ versus temperature. The insets show detailed stress distribution in the film at different temperatures (The 2D maps are a plot of $-\sigma'_{zz} = \sigma'_{xx} + \sigma'_{yy}$ as a measure of the in-plane stress). Note the blue regions of compressive stress in the 105 ºC map, while on average the stress is still in the tensile regime.

A plot of the average biaxial stress in the blanket film obtained by x-ray microdiffraction during a thermal cycle between 25°C and 345°C is shown in Fig. 1. The stresses in approximately 130 grains in a 15μm x 15μm region were averaged to give the results shown in the figure. Though our temperature range is about 100°C smaller, the temperature cycling curve using microdiffraction is very similar to that reported by Venkatraman et al [3] using wafer curvature measurements on an Al(Cu) films with thickness 1 μm. The film is in tension at room temperature, with an average biaxial stress of 230 MPa. The measured stress is caused by mismatch between the thermal expansion coefficients of the aluminum and the silicon substrate. Upon heating, the higher thermal expansion coefficient of the aluminum film relaxes the tensile stress before driving the film into compression. From Fig. 1 the experimentally determined initial thermoelastic slope is $(d\sigma / dT) = 2.53$ MPa / °C. The theoretical thermoelastic slope was calculated to be 2.34 MPa / °C, in reasonable agreement with the experimental value.

The real advantage of using μSXRD is however the possibility to obtain orientation and strain/stress information at a very local level, allowing for the study of mechanical properties of thin films with new visibilities. For instance, it provides a simple and straightforward explanation to the early departure from linearity of the thermoelastic slope during heating (seen in [3] as well as in the present data), even before the film enters in the compressive state. At room temperature, the stress is highly inhomogeneous with regions sustaining more tensile stress than others. Upon

heating some regions of the film become compressive while the average biaxial stress is still in the tensile regime. Even though the average stress is zero at about 100°C some grains have already reached their yield stress and deformed and the heating curve departs from linearity. The temperature at which the curve departs from linearity is quite variable for different films and depends on detailed process parameters.

Similar local variations of the stress are observed in the passivated lines. These local variations increase with decreasing line width while the area of the hysterisis of the stress-temperature curves decreased. The hysteresis area is typically a measure of the amount of plastic deformation experienced by the material. In the case of submicron sized lines, the passivation layers introduce additional constraints to the dislocation motions, as compared to the case of unpassivated blanket films [4]. These local stress variations which do not always follow grain boundaries but can be intragranular, are quite surprising in an elastically isotropic material as aluminum. However these differences can be explained by differences in grain sizes and grain-to-grain interactions [5].

ACKNOWLEDGMENTS

The authors thank Intel Corp. for the partial funding of the end station.

REFERENCES

1. A. A. MacDowell, R. S. Celestre, N. Tamura, R. Spolenak, B. Valek, W. L. Brown, J. C. Bravman, H. A. Padmore, B. W. Batterman, and J. R. Patel, Nucl. Instr. & Meth. In Phys. Res. **A 467-468**, 936 (2001).
2. N. Tamura, R. Spolenak, B.C. Valek, A. Manceau, N. Meier Chang, R.S. Celestre, A.A. MacDowell, H.A. Padmore and J.R. Patel, Rev. of Sci. Instr., **73** (2002) in press.
3. R. Venkatraman, J. C. Bravman, W. D. Nix, P. W. Davies, P. A. Flinn, D. B. Fraser. J. of Electron. Matls. **19**, 1231 (1990).
4. B.C. Valek, N. Tamura, R. Spolenak, A.A. MacDowell, R.S. Celestre, H.A. Padmore, J.C. Bravman, W.L. Brown, B. W. Batterman and J. R. Patel, Mat. Res. Soc. Symp. Proc., **673**, P.7.7.1 (2001).
5. R. Spolenak et al. (2002) this compendium.

This work was supported by the Director, Office of Science, Office of Basic Energy Sciences, Materials Sciences Division, of the US Department of Energy under Contract No. DE-AC03-76SF00098 at Lawrence Berkeley National Laboratory.

Principal investigator: Nobumichi Tamura, Advanced Light Source, Ernest Orlando Lawrence Berkeley National Laboratory. Email: NTamura@lbl.gov. Telephone: 510-486-6189.

In-situ Synchrotron X-ray Microdiffraction Study of Deformation Behavior in Copper-Polycrystals during Uniaxial Deformations

H.D. Joo[1], J.S. Kim[1], K. H. Kim[1] , N. Tamura[2], and Y. M. Koo[1]
[1] *Center for Advanced Aerospace Materials, Dept. Materials Science & Engineering, Pohang University of Science and Technology, Pohang 790-784, South Korea*
[2] Lawrence Berkeley National Laboratory, University of California, Cyclotron Road, Berkeley, CA94720, USA

INTRODUCTION

Recent experiments have shown that the plastic deformation and the fracture of solid have relation with the formation of dislocation cell structure and the rotation of structural elements[1]. Therefore, attention should be focused on a mesovolume of deformed material. Because The local stress and strain differ from those averaged at the macroscale, the discrete nature of the micro-deformation of the mesofragments should be accounted for the rotation of the different mesofragments being parts of subgrain, a grain, grains, etc., which plays an important role in plasticity. Moreover, In-situ study of deformation behavior in polycrystalline material during deformations at microlevel had not been performed. In the present work, we have investigated plastic deformation behavior in polycrystalline material during deformations at microlevel using the X-ray Microdiffraction technique on beamline 7.3.3. at the ALS. This technique allows the measurements of local orientation and strain in microvolume element within a grain. In addition, an accuracy of this technique is about $2x10^{-4}$ in strain and less than 0.01^{o} in orientation[2].

EXPERIMENT

The material used in the present study was a 99.999% pure polycrystal of copper. A tensile sample, with a gauge length of 7.5mm and a cross-section of 2x0.5 mm, was prepared by spark-erosion cutting. After mechanical polishing, the sample was annealed in a vacuum at 600□ for 30min. and chemically polished to remove damaged and oxidized surface material formed during mechanical polishing and heat treatment.

The synchrotron radiation source of beam line 7.3.3 at the Advanced Light Source (ALS) was used for the *in situ* Microdiffraction Laue experiment, described in [2,3]. In order to measure Orientation and strain/stress distributions at each strain(0, 2, 4, 6, 8, 10, 15, 20, 25, 30% strain), a large number of diffraction pattern are collected by scanning the sample and analyzed. The beam size of experiment was 1.5μm x 1.5μm and the detector was a charge-coupled device camera. The samples were elongated in steps of 0.15 mm by a tensile device mounted on the translation stage. The strain rate was $2.22x10^{-4}$.

RESULTS AND DISCUSSION

Figure 1 shows the orientation distribution of Copper sample at each deformation step(0, 2, 4, 6% strain). The tensile direction is vertical in the plots. The orientation of big center grain starts to change starting in the middle of the grain as the tension applied. In order to consider the heterogeneities of the deformation-induced microstructure within single grains, tensile axis rotation in other position within a grain is measured. We take five local positions in center grain which are Ag, Bg, Cg, Dg and Eg position, and measure the tensile axis rotation at each point. Figure 2(a) shows positions of 5 points.

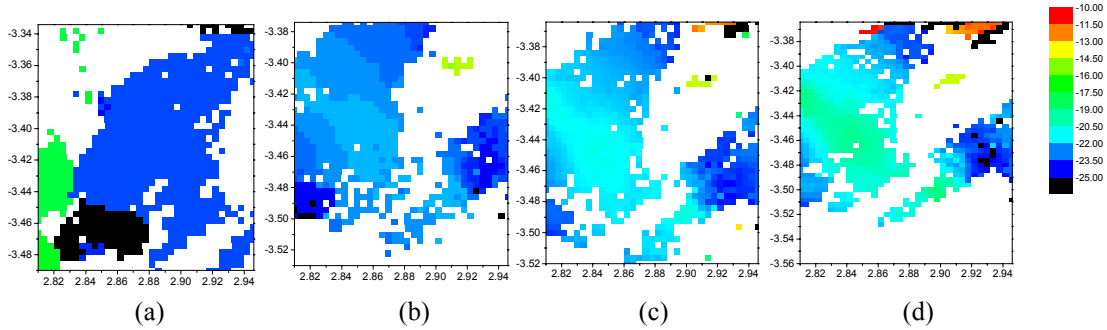

Fig.1.Grain Orientaion distribution of Copper sample at each deformation step((a)0, (b) 2, (c) 4, (d) 6% strain).

Figure 2(b)(c) shows rotation angle from initial position as a function of strain at each strain, and the orientation of neighbor grains in standard triangle, respectively. The tensile axis rotation at Ag position is larger than that at Dg position. The initial orientation of grain 2,8 near Ag position is similar to that of center grain while the angle between grain 5,6 and center grain is quite large. That is, the grain boundary in diagonal direction is small angle boundary. In the orientation map, primary slip direction ($\bar{1}01$) at sample coordination is (0.172,-0.363, 0.378) which is a diagonal direction in the plot. This phenomenon may be due to differences in the selection of simultaneously acting slip systems among neighboring volume elements of individual grains and different part of grain interior. Lattice rotation near high angle grain boundary is large while Lattice rotation near low angle grain boundary is small. This means that Grain boundary and grain orientation affect the slip behavior.

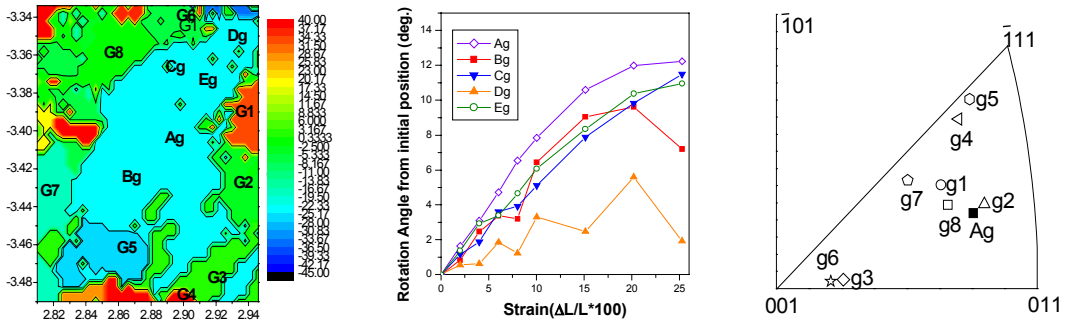

(a) (b) (c)

Fig.2. (a) shows positions of 5 points,(b)(c) shows rotation angle from initial position as a function of strain at each strain, and the orientation of neighbor grains in standard triangle, respectively.

REFERENCES

1. N.Hansen, Mater. Sci. Engng. **6**, 1039 (1990).
2. A. A. MacDowell, R. S. Celestre, N. Tamura, R. Spolenak, B. Valek, W. L. Brown, J. C. Bravman, H. A. Padmore, B. W. Batterman and J. R. Patel, Nuclear inst. Meth. **467-468**, 936 (2001).
3. N. Tamura, R. Spolenak, B.C. Valek, R.S. Celestre, A.A. MacDowell, H.A. Padmore and J.R. Patel, **"**Orientation and Stress Mapping on Beamline 7.3.3.: a New Tool to Study Material Properties at Submicron Scale", ALS activity report 2000.

This work was supported by POSTECH (Pohang University of Science and Technology) and materials analysis team of RIST(Research Institute of Industrial Science & Technology)

Principle investigator: H.D. Joo, Center for Advanced Aerospace Materials, Pohang University of Science and Technology, e-mail:matter@postech.ac.kr, Telephone: 82-54-279-5130.

Lateral inhomogeneities and termination in ultrathin block copolymer films

R. Fink[1], Th. Schmidt[1], N. Rehse[2], G. Krausch[2], I. Koprinarov[3], H. Ade[4]

[1]Experimentelle Physik II, Universität Würzburg, Am Hubland, D-97074 Würzburg, Germany
[2]Physikalische Chemie II, Universität Bayreuth, D-95440 Bayreuth, Germany
[3]Brockhouse Institute for Materials Research, McMaster Univ., Hamilton, ON L8S 4M1, Canada
[4]North Carolina State Univ., Dept. Of Physics, Raleigh, NC 27695 , USA

INTRODUCTION

Linear chain-like molecules consisting of blocks of chemically different components (so-called block-copolymers) in many cases form long-range ordered supramolecular structures. The reason for this behavior is the interplay between phase separation of the different components and the molecular unity in the single molecules. The size of the forming structures depends on the size of the molecules and ranges from about 10 to 100 nm. This is usually called "microphase separation" or "micro domain formation". Due to the differences in the surface free energy of the polymers the structure of the micro domains of the surfaces and interfaces can be manipulated. Whereas the structure and morphology of diblock copolymers has been intensely investigated, the investigation of more complex structures (multiblock copolymers, graft polymers, star-like copolymers, etc.) has started only recently.

Recent investigations demonstrate more complex surface and thin film morphologies [1-3]. E.g., an ABC-triblock copolymer consisting of polystyrene (PS), polybutadiene (PB) and polymethylmethacrylate (PMMA), which forms lamellar-like structures in bulk, forms lateral structures at the surface, since the PB-center block (PB) has the lowest surface free energy [4]. To investigate these structures, microscopic techniques with none or only limited spectral sensitivity have been employed so far (atomic force microscopy, scanning electron microscopy, transmission electron microscopy). Although these techniques offer a limited potential to distinguish the polymer blocks, a definite and unambiguous attribution of the respective polymer subunits is still lacking.

EXPERIMENTS

We have used the unprecedented opportunities of high brilliance synchrotron radiation at the Advanced Light Source in particular the installed microspectroscopes (PEEM2 at BL 7.3.1.1 and STXM at BL 7.0.1) to investigate the stoichiometric inhomogeneities in those films within the bulk (STXM) and in the surface-near region (PEEM). Our preliminary experiments have explicitely demonstrated the usefulness of these microspectroscopic techniques.

Fig. 1 shows a STXM image of a thin film consisting of a PS-PB-PMMA triblock copolymer (floated on a 100 nm thick Si_3N_4 membrane) recorded at a photon energy of 293 eV (image size: 60 x 60 μm^2). The lower image shows a cross section along the red bar clearly indicating the distinct film thicknesses in the sample. This finding is in accordance with the lamellar structure which is formed in bulk of those materials. Brighter spots give a clear indication of an additional lateral fine structure within the homogenous areas. The structures in the upper left corner of Fig. 1 are due to partial dewetting of single terraces.

Fig. 2 shows two XPEEM images recorded at the positive and negative slope of the prominent π^*-resonance ($h\nu$ = 286.5 eV) reflecting a distinct contrast reversal which ist due to the different termination of the various terraces, i.e. in one case the terrace consists mainly of the PS species whereas in the other areas PMMA is the prominent species. Images recorded at the O K-edge

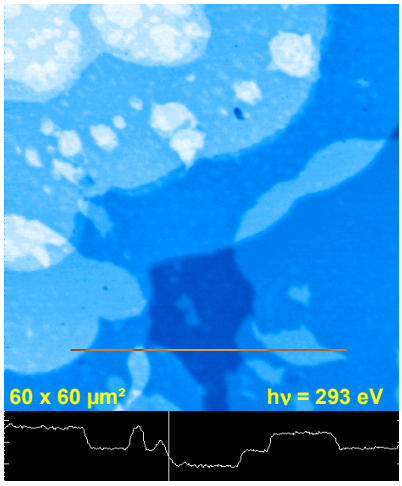

Fig.1: STXM image of a PS-PB-PMMA-triblock copolymerfilm.

allow much higher magnification due to the higher photon flux and thus allow direct imaging of the lateral patterning, which is dominated by the dewetting of the organic film. The finding of differently terminated areas is fully consistent with previous indirect conclusions drawn from AFM data and thus represents a direct spectroscopic proof.

In both cases, PEEM and STXM, the microdomain formation within a terrace with periodicities on the order of up to several 10 nm can at present not be resolved. XPEEM of soft matter films at present is limited to lateral resolutions of about 100 nm and, in addition, may lead to misinterpretations of the spectroscopic data since the high photon flux densities lead to fast degradation/fragmentation of the organic molecules or even conversion into graphite. STXM partly overcomes the latter restriction since the illumination time is significantly shorter. Much higher transmission (by a factor 100 to 1000 at comparable magnification) of the electron optics in an aberration-corrected XPEEM (like, e.g., at PEEM3 or SMART) will improve spectroscopic imaging of surfaces of soft matter films.

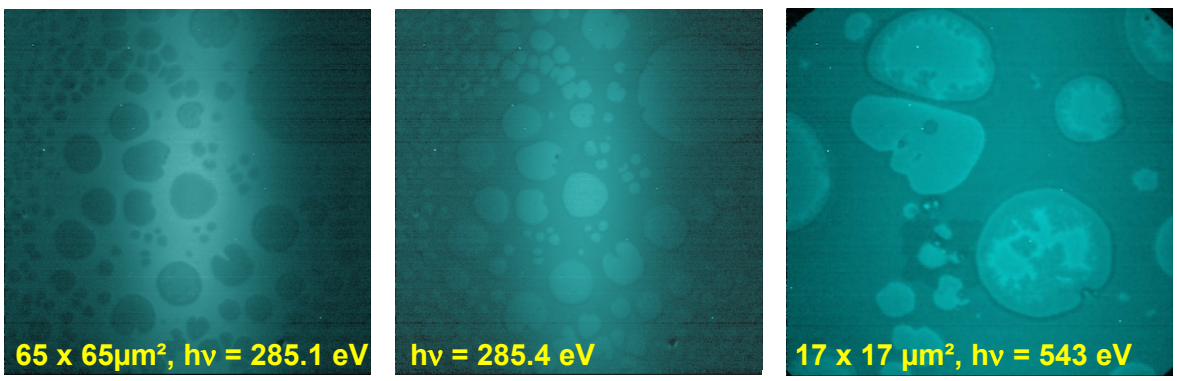

Fig. 2: PEEM images of a PS-PB-PMMA triblock copolymer film indicating the spectroscopic contrast (contrast reversal in the XPEEM images by 0.3 eV photon energy variation). Left and center: excitation at the C K-edge; right:excitation at the O K-edge at higher magnification.Note, that the surface has been plasma-etched to remove the top PB layer.

REFERENCES

[1] W. Stocker, J. Beckmann, R. Stadler, J.P. Rabe, *Macromolecules* **29,** 7502 (1996).

[2] H. Elbs, K. Fukunaga, G, Sauer, R. Stadler, R. Magerle, G. Krausch, *Macromolecules* **32,** 1204 (1999).

[3] K. Fukunaga, H. Elbs, G. Krausch; *Langmuir* **16,** 3474 (2000).

[4] N. Rehse, A. Knoll, R. Magerle, G. Krausch; *Phys. Rev. Lett.* **87.** 035505 (2001)

This work was supported by the Bundesminister für Bildung und Forschung, contracts 05SL8WW18 and 05KS1WCA1. We gratefully acknowledge experimental support by A. Scholl and A. Doran during the experiments at PEEM2. Many thanks to A.P. Hitchcock for providing the AXIS 2000 program for data evaluation.

Principal investigator: Rainer Fink. Experimentelle Physik II, Universität Würzburg.
Email: raifi@physik.uni-wuerzburg.de Telephone: +49-931-888-5163.

Magnetic Switching by Spin Injection

C. Stamm[1], S. Andrews[2], A. Scholl[3], C. T. Rettner[4], J.-U. Thiele[4], J. Stöhr[1]

[1]Stanford Synchrotron Radiation Laboratory, Stanford, CA 94309, USA
[2]Material Science and Engineering, Stanford University, Stanford, CA 94305, USA
[3]Lawrence Berkeley National Laboratory, Berkeley, CA 94720, USA
[4]IBM Almaden Research Center, San Jose, CA 95120, USA

INTRODUCTION

Spin-polarized currents provide a new method of efficiently manipulating nanoscale magnetic domains utilizing the short range and strong electronic exchange interaction. The spins of the injected electrons generate a torque on the magnetization of a ferromagnetic film, which at sufficiently high current densities is capable of switching a magnetic domain. We have started a program to directly observe the magnetic switching process during the spin injection process by means of static and time resolved photoemission electron microscopy utilizing the PEEM-2 microscope on beamline 7.3.1.1.

SAMPLES

One crucial parameter for successful switching by spin injection is a high current density. This can be easily achieved when the current flow is restricted to nano-contacts. In our samples, several 50 nm diameter channels are drilled into a 30 nm thin Si_3N_4 membrane using a focused ion beam. These holes are then filled by copper deposition from both sides, forming nano-contacts. The sample structure and preparation is illustrated in Figure 1.

When a voltage is applied between the front and the back of the membrane, the current has to pass through these nano-contacts. This gives rise to a high current density at the location of the channels, falling off inside the film with distance from the center. A spin polarized current is generated by passing the electrons through a ferromagnetic thin film "polarizer" that is aligned unidirectionally by exchange bias. The "polarizer" is decoupled from a second ferromagnetic thin film "sensor" by a copper interlayer, so the two films are magnetically independent. The micromagnetic configuration of the "sensor" film, which is deposited on top of the structure, is then observed with PEEM-2 as a function of the spin polarized current density.

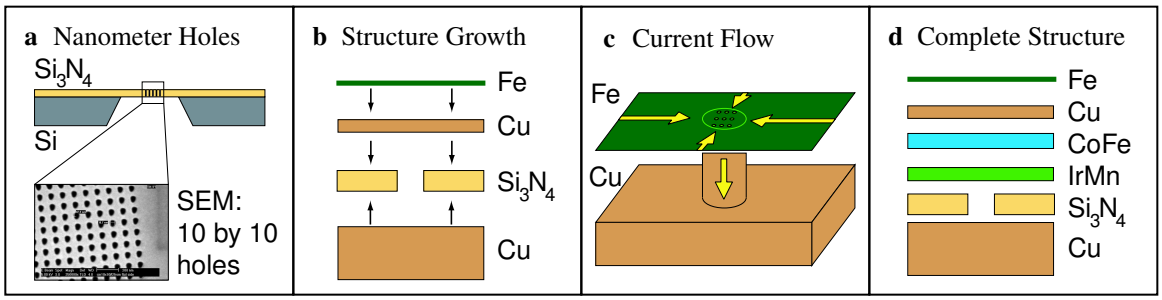

Figure 1: Sample structure for spin injection experiment. **a**: several 50 nm diameter holes are drilled into a Si_3N_4 membrane using a focused ion beam. **b**: Cu is then deposited from both sides, forming nano-contacts. **c**: a current is passed through the Cu filled channels in the membrane and the thin films. **d**: the complete structure, utilizing an exchange biased CoFe/IrMn film as electron polarizer, a Cu buffer layer, and a Fe sensor layer.

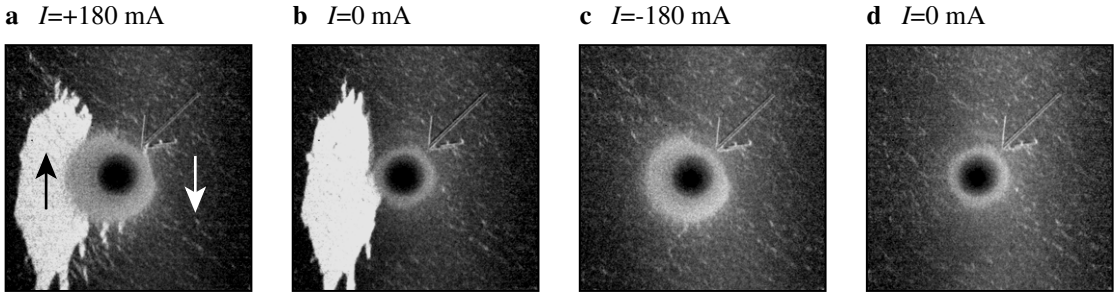

Figure 2: PEEM image at Fe L_3 peak divided by image at Fe L_2 in order to obtain magnetic contrast. The image size is 45 μm. The magnetic axis is along the vertical direction, white corresponds to up and black corresponds to down magnetization (see arrows in **a**). An arrow on the sample points towards the location of the Cu channels. The image series corresponds to different currents through the sample: **a**: the current is able to generate a white domain, which was not present before, it stays when the current is turned off (**b**). **c**, **d**: by reversing the current direction the domain vanishes.

PRELIMINARY RESULTS

First measurements were performed on a sample consisting of Cu channels with a single 8 Å thick magnetic Fe film on top, as shown in Figure 1**b**. A rather large current of up to 180 mA (corresponding to a current density of $j \approx 10^{12}\mathrm{A/m^2}$) was passed through 100 Cu filled channels in the membrane, which destroyed the center region locally (dark circle). However, the measurement demonstrated that the current passes through the Cu channels, and that imaging with PEEM-2 is possible during the injection of a current. The observed switching of a white domain on the left of the channels is due to Oersted-type fields generated by the current. A gray ring around the center region indicates heat generation: the local temperature reached the Curie point, causing loss of magnetic signal.

This work was supported by the Materials Science Division, Office of Basic Energy Sciences of the U.S. Department of Energy.

Contact person:
Christian Stamm, Stanford Synchrotron Radiation Laboratory, M/S 69,
2575 Sand Hill Road, Menlo Park, CA 94025, USA
Email: stamm@slac.stanford.edu, Telephone: 650-926-3042

Microstructure and pinning properties of hexagonal-disc shaped single crystalline MgB_2

C. U. Jung[1], J. Y. Kim[1], P. Chowdhury[1], Kijoon H. P. Kim[1], Sung-Ik Lee[1], N. Tamura[2], W. A. Caldwell[2], and J. R. Patel [2,3]

[1]National Creative Research Initiative Center for Superconductivity and Department of Physics, Pohang University of Science and Technology, Pohang 790-784, Republic of Korea

[2]Lawrence Berkeley National Laboratory, Advanced Light Source, 1 Cyclotron Road, MS-2-400 Berkeley, CA 94720, USA

[3] SSRL/SLAC, Stanford University, CA 94309, USA

INTRODUCTION

The existence of impurities and structural imperfections on a microscopic scale can result in diverse transport and pinning properties in MgB_2, which was even observed for single crystalline samples made by several groups[1-3]. Here, we report the X-ray micro-diffraction measurements for, MgB_2 single crystals with hexagonal-disc shapes and shiny surfaces. The diagonal length and the thickness for the largest crystal was about 100 μm and 10 μm, respectively. The crystallinity was thoroughly identified by using the Laue pattern in the X-ray micro-diffraction measurement. Both the edge and the c-axis of the hexagonally shape disc were found to match the crystal symmetry.

EXPERIMENTAL

Two different procedures were used to grow the single crystals, and in both cases, excess Mg was critical for the growth of single crystals. The first involved a two-step method in which already synthesized pieces of MgB_2 bulk[4] were used as a seed material. They were heat treated in a Mg flux inside a Nb tube, which was sealed in an inert gas atmosphere. Then, the Nb tube was put inside a quartz tube, which was sealed in vacuum. The quartz tube was heated for one hour at 1050 °C, cooled very slowly to 700 °C for five to fifteen days, and then quenched to room temperature. The crystal images were observed using a polarizing optical microscope and a field-emission scanning electron microscope (SEM). We successfully separated single-crystalline MgB_2 from the Mg flux by using a thermo-mechanical spinning method.

For the X-ray micro-diffraction measurements, several crystals were fixed at the center of Cu crosshairs on the substrate, as shown in Fig. 1. The instrument used at the Advanced Light Source (ALS) for X-ray micro-diffraction is capable of producing a submicron-size X-ray microbeam and with submicron spatial resolution can probe the local texture in a single crystal[5]. The sample was positioned using the Cu fluorescence signal detected from the Cu crosshairs on the Si substrate by using a high-purity Ge ORTEC solid-state detector connected to a multichannel analyzer. The crystal orientation with respect to the substrate can be determined with an accuracy of 0.01 degree.

RESULTS

The crystal structure was identified by using white beam X-ray micro-diffraction measurements. After positioning these single crystals, a 100 μm × 100 μm region between the Cu crosshairs was scanned with a step size of 2 μm. At each step, the Laue pattern (together with the Cu *K*

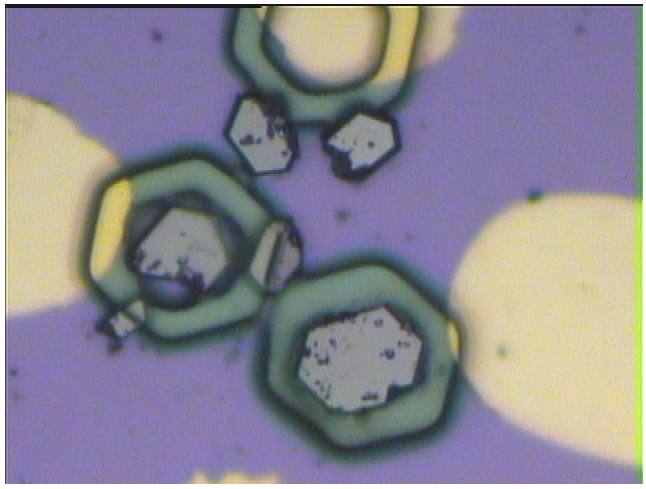

Figure 1. Polarizing optical microscope images of MgB_2 single crystals. An epoxy was used to fix six single crystals at the center of 100 μm-wide Cu crosshairs.

fluorescence signal) was collected with a BRUKER 6000 CCD camera which has an active area of 9 × 9 cm and was placed about 4 cm above the sample. [2500 images, 1024 pixel ×1024 pixel mode] The exposure time at each step, was 1 second. An example of a Laue pattern obtained from a MgB_2 single crystal is shown in Fig. 2(a). The Laue patterns are consistent with a hexagonal MgB_2 structure (a =0.3086 nm, c = 0.3524 nm, Space Group number =191, Ref. 6). The (0005) reflection in the center of the pattern in Fig. 2(a) corresponds to the direction of the normal to the crystal surface. This confirms that the surface plane normal is along the c-axis. Moreover, the hexagonal edges of the crystals were found to match the <1,0,-1,0> directions within a fraction of a degree resolution. Thus, the shapes of the crystals in the microscope image followed the MgB_2 crystal symmetry, which will be quite useful for any research of the direction dependencies of the physical properties in MgB_2.

Indexing the Laue patterns in Fig. 2(a) allowed us to calculate the complete orientation matrix of the X-ray illuminated volume. A finer step size of 1 μm was used for the white-beam scan. The orientation variations inside the single crystal shown in the right bottom corner of Fig. 1 are shown in Figs. 2(b) and 2(c). Figure 2(b) is the out-of-plane orientation variation calculated as the angle between the c-axis and the normal to the surface of the silicon substrate. The out-of-plane variation was about 0.2 degrees between the light orange and the red regions. The out-of-plane orientation shows a variation of about 0.2 degrees between the bottom and the top parts, indicating a slight bending of the crystal (which might be due to the photoresist used as an epoxy). Figure 2(c) shows the in-plane orientation variation calculated as the angle between the measured a-axis (or b-axis) and a reference directions. The variation was about 0.4 degrees between the light blue-green and the green regions. The in-plane orientation also showed some inhomogeneities of up to about 0.2 degrees.

These results demonstrate that the orientation of crystal axis of our hexagonal-disc-shaped single crystals was perfect, within 0.2 degrees[7]. A recent study showed that (0001) twist grain-boundaries, formed by rotations along the c-axis (typically by about 4 degrees), were the major grain boundaries in polycrystalline MgB_2 [8].

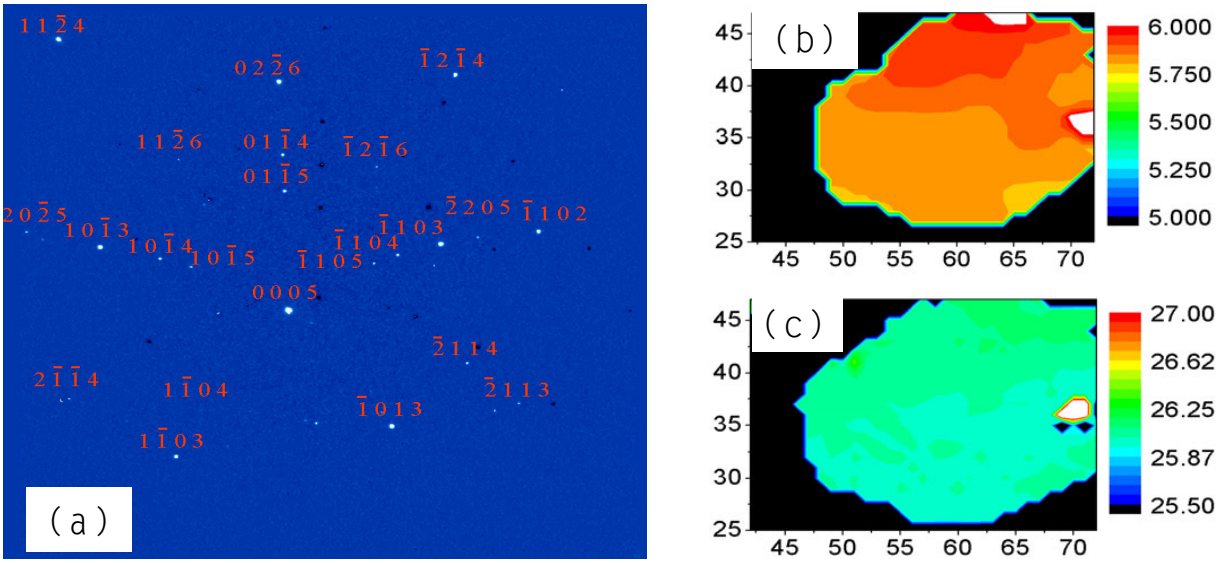

Figure 2. (a) A representative image of an indexed Laue pattern from X-ray micro-diffraction. (b) and (c) are, respectively, for the out-of-plane and the in-plane orientations inside a single crystal.

REFERENCES

1. S. Lee, H. Mori, T. Masui, Yu. Eltsev, A.Yamamoto, and S.Tajima, J. Phys. Soc. Jpn. **70**, 2255 (2001).
2. M. Xu, H. Kitazawa, Y. Takano, J. Ye, K. Nishida, H. Abe, A. Matsushita, N. Tsujii, and G. Kido, Appl. Phys. Lett. **79**, 2779 (2001).
3. O. F. de Lima, R. A. Ribeiro, M. A. Avila, C. A. Cardoso, and A. A. Coelho, Phys. Rev. Lett. **86**, 5974 (2001).
4. C. U. Jung, Min-Seok Park, W. N. Kang, Mun-Seog Kim, Kijoon H. P. Kim, S. Y. Lee, and Sung-Ik Lee, Appl. Phys. Lett. **78**, 4157 (2001)
5. A. A. MacDowell, R. S. Celestre, N. Tamura, R. Spolenak, B. C. Valek, W. L. Brown, J. C. Bravman, H. A. Padmore, B. W. Batterman, and J. R. Patel, Nucl. Instrum. Meth. A **467-468**, 936 (2001).
6. J. Nagamatsu, N. Nakagawa, T. Muranaka, Y. Zenitani, and J. Akimitsu, Nature **410**, 63 (2001).
7. C. U. Jung *et al*., to be submitted to Phys. Rev B.
8. Y. Zhu, L. Wu, V. Volkov, Q. Li, G. Gu, A. R. Moodenbaugh, M. Malac, M. Suenaga, and J. Tranquada, Physica C **356**, 239 (2001).

The work done at the Advanced Light Source is supported by the Director, Office of Science, Office of Basic Energy Sciences, Materials Sciences Division, of the U.S. Department of Energy under Contract No. DE-AC03-76SF00098 at Lawrence Berkeley National Laboratory. Part of work done at PSC is supported by the Ministry of Science and Technology of Korea through the Creative Research Initiative Program.

Principal investigator: Nobumichi Tamura, Advanced Light Source, Ernest Orlando Lawrence Berkeley National Laboratory. Email: ntamura@lbl.gov. Telephone: 510-486-6189.

Optimization of PEEM-2 for studies of organic thin films

C. Morin[1], A.P. Hitchcock[1], H. Ikeura-Sekiguchi[1,2], A. Scholl[3], A. Doran,[3] K. Kaznacheyev[4]
[1]BIMR, McMaster University, Hamilton, ON, Canada L8S 4M1
[2]Quantum Radiation Division, Advanced Industrial Science and Technology (AIST), Tsukuba, 305-8568 JAPAN
[3]Advanced Light Source, Berkeley Lab, Berkeley, CA 94720
[4]Physics, CLS, University of Saskatchewan, Saskatoon, SK Canada S7N 5C6

INTRODUCTION

There are many potential applications of X-ray photoelectron emission microscopy (X-PEEM) to organic thin films, such as fundamental studies of phase separation [1], and applied studies of organic light emitting diodes, adhesion promoters [2] etc. In order to obtain meaningful results, it is important to understand the challenges of applying X-PEEM to organics, and to develop compensating data acquisition strategies. These challenges include: radiation damage, camera artifacts, Io determination, higher order radiation, charging, sample damage from field emission or discharges.

The photon flux at BL 7.3.1 ($>10^{12}$ photons/s at 500 eV in a 30x300 μm spot, with 1.9 GeV, 400 mA) is very high because there are only two optical elements and energy resolution is sacrificed for flux. The high flux, combined with a relatively inefficient electrostatic column (~5 % transmission at high spatial resolution – 12 μm aperture) and an inefficient camera, mean that ratio of detected signal to number of photons absorbed in the near surface region is very small. In order to perform useful chemical analysis, images of the region of interest must be recorded at a number of energies (in the C1s, N1s or O1s regions for organic samples) to form an image sequence which can be subsequently analysed to obtain point or region spectra, or chemical maps. Other problems occur because of limitations of the CCD camera - bad pixels; pixel-to-pixel variation in dark signal (leakage) and gain; as well as a slow data transfer rate (0.25s/image, no ability to transfer sub images). A further challenge is the uneven illumination in the PEEM; in order to gain sensitivity we use reduced magnification. Typically the camera views 60x60 μm^2 but only the central third of the image is illuminated.

In order to reduce the damage rate we work at much reduced flux, achieved by placing an aperture (formed by two independently adjustable elements, called 'chopper' and 'mask') in the beam before the monochromator. This reduces the energy resolution as well as the flux – at a chopper value of 15 the resolving power is only 100. Under typical low dose conditions we work with less than 10% of the dynamic range of the camera. Background and camera corrections are extremely challenging. It is essential to record Io spectra from a suitable reference surface, typically HF-etched silicon for organic thin film samples deposited on Si or Si_3N_4. This is especially true in the C 1s region where there is a lot of structure in the Io spectrum. The Io signal must be measured under very similar conditions to those used to study the sample in order to ensure the same sensitivity, energy resolution and higher order content, (the latter two depend on the exact choice of chopper, windows, slits and filters used). The PEEM sensitivity is very dependent on the sample-objective lens distance, which changes every time a sample is re-positioned.

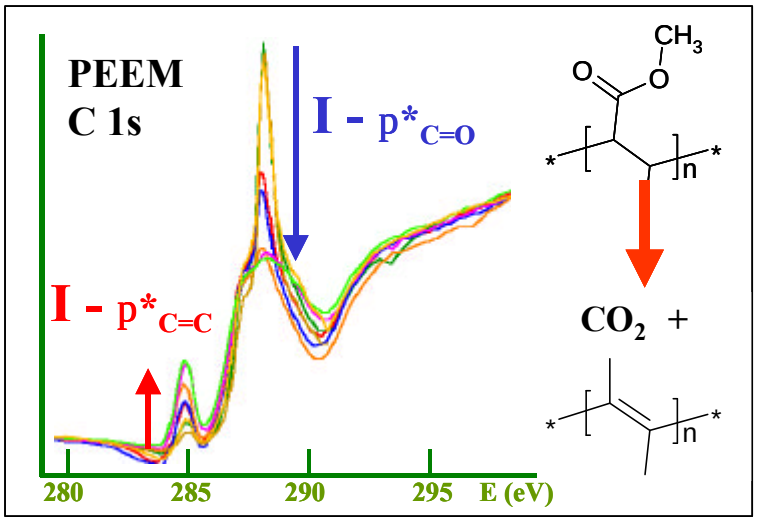

Fig. 1 Plots of C 1s NEXAFS of a 50 nm PMMA film on c-Si. Successive scans made on the same spot build up dose and damage.

Charging can occur for any insulating sample, although it is often surprising the samples that can be studied by PEEM. We typically observe charging if a polymer sample is too thick (> 75 nm), or too corrugated (> 15 nm rms). In some cases a thin metal coating (<2-3 nm) can be evaporated to control charging. Charging results in dark spots on images, where the electrons are trapped by the surface charge potential, or in bright spots, where there is artificially enhanced emission by discharges or, at locations of high curvature, by enhanced detection

probability due to stronger fields. While it is sometimes possible to record meaningful NEXAFS spectra from charging surfaces, more typically, charging results in large and variable sample or objective lens currents which lead to unstable operation, and, in extreme cases, macroscopic discharges that can damage samples, making dramatic dendritic patterns in organic layers, and exploding Si_3N_4 windows. In the following we describe a systematic study of a pure polymethylmethacrylate (PMMA) film in order to characterize its radiation damage rate, and thereby develop procedures to study heterogeneous samples containing PMMA in a meaningful fashion, despite these challenges. A detailed manual for operating X-PEEM and choosing parameters optimal for radiation sensitive samples is available at the beam line or from the authors [3].

EXPERIMENTAL

~50 µl of a 1.0% w/w toluene solution of PMMA (Mw = 112.3 K, Mw/Mn = 1.09, Polymer Source Inc) was passed through a teflon filter to remove particulate impurities and dropped onto a spinning HF-etched Si chip at 4000 rpm. Spinning was continued for ~5 s. The film thickness was estimated to be ~40 nm from AFM at a scratch and the rms roughness was 6 nm The sample was not annealed.

Property	Value	Property	Value
Mask	0.9	Dwell (s)	3
Chopper	15 or 16	Camera gain	normal, x8
Al window #1	in	PEEM aperture (µm)	50
Al window #2	in	Sample (kV)	18.0
Exit slit	in	Objective (kV)	13.68
Ti filter (150 nm)	in	Transfer (kV)	12.45
Flash light	on	Intermediate	13.78
Background (Hz)	50	Projection	0

The relationship of measured intensity to the various parameters controlling the signal is summarized in **equation 1**. A number of scale factors need to be determined but this qualitative formula may be useful for others using PEEM-2 for organic thin film studies.

$$S = G*t*[I*\sigma*f_{esc}*F*\varepsilon_{PEEM} - B] \qquad \text{(eqn 1a)}$$

where S = detected signal , G = camera gain (2,4,8), t = time, σ = cross-section, f_{esc} = electron escape probability (integrated over inelastic scattering and angular effects), F = work function, ε_{PEEM} = PEEM column efficiency [α (magnification)* (aperture)^2], B = no-X-ray background, and I is the flux (ph/s) on the sample, given by

$$I \propto I_{ring}*C*T \qquad \text{(eqn 1b)}$$

where C, the chopper factor is $(C_{max}-C)/C_{max}$; and T, the Ti filter factor, is $(T_{max}-T)/T_{max}$.

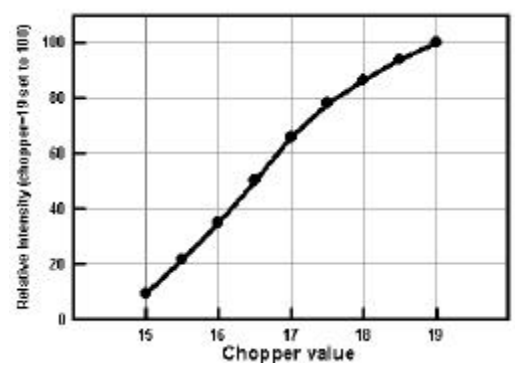

Fig. 2 Variation of flux on sample vs. chopper.

RESULTS AND DISCUSSION

Fig. 1 shows a typical sequence of spectra (without Io correction) recorded while the sample was being damaged. The relative radiation damage rate for PMMA in the low dose regime was determined by recording successive image sequences on the same spot, using the instrumental parameters listed in table 1. Only 24 energies in 283-295 eV range were used in order to track damage changes adequately. In general keeping the number of sampled energies to the minimum is a key step in making meaningful measurements of organics. The *relative dose* was obtained from the integrated spectral signal up to a given measurement, taking into account the dead time between images (~2 s). The *relative damage* was obtained from the increase in the area of the 285 eV $\pi^*_{C=C}$ peak (growth of reduced sites in the backbone) and decrease in the area of the 288 eV $\pi^*_{C=O}$ peak (loss of acrylate groups). In addition to the measurements made at low dose, another series at much higher dose (5 or 10 s exposure at chopper 19) was performed. The two sets were matched in the overlapping region of the 285 eV and 288 eV damage curves. Finally the dose scale was expressed in terms of time equivalent at full flux in the carbon 1s region using the variation of signal strength with chopper setting to scale the times (**Fig. 2**).

Fig. 3 plots damage versus relative dose for PMMA as measured in the PEEM As is typical in radiation damage curves, there is an exponential change with saturation. Based on these results, we estimate that, at the full flux dose rate (chopper = 19, 400 mA in the ALS), the total acceptable exposure time for meaningful measurements of samples containing PMMA with negligible damage (as measured by spectral change) is 10 seconds. Since it takes about 5 seconds to record an image of acceptable quality, if full flux is used it is only possible to record a few images before the PMMA in a PMMA-containing sample is irreversibly modified. We note that a recent study of radiation damage in various polymers by STXM [4] indicates that PMMA is about average in terms of radiation sensitivity.

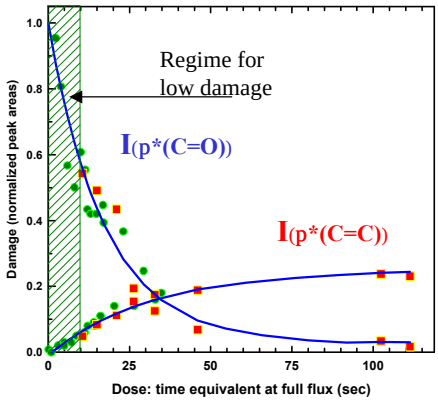

Fig. 3 Intensity at 288 eV and 285 eV versus accumulated radiation dose. The dose is time to equivalent deposited energy when PEEM is operated with full flux. The green points are measurements made at reduced flux. Chopper: green (15), red (19).

Chemical imaging with PEEM requires images at a number of energies.Typically 10-15 images are needed. The only way to get these without "frying the sample" is to "turn down the torch". We routinely do this by using the chopper to reduce the flux ~10-fold (see Fig. 2). This allows 10-20 images to be recorded prior to significant damage. Chopper values below 15 are not useable since the grating is inadequately illuminated. 2-bunch mode is also useful, but normalizing the rapid time variation of flux is a challenge.

Fig. 4 presents results of a low dose study of a 20:80 (w/w) PS:PMMA film (PS = polystyrene) which has domain sizes on the order of 250 nm as determined by prior AFM measurements. This is a continuation of our earlier studies of phase segregation on PS:PMMA blends [1]. We are trying to develop a metastable system with flat, reasonably large domains that are pure PS and PMMA, in order to carry out competitive protein adsorption studies. As the analysis of the spectrum of the PMMA-rich regions shows, the as-made material still contains significant PS, as found earlier [1]. However, with our refined understanding of the damage rate of PMMA in PEEM-2, we are now very confident that the 285 eV signal observed in the PMMA-rich domains is from incompletely phase segregated PS and NOT from the C=C bonds formed from radiation damage of PMMA (Fig 1).

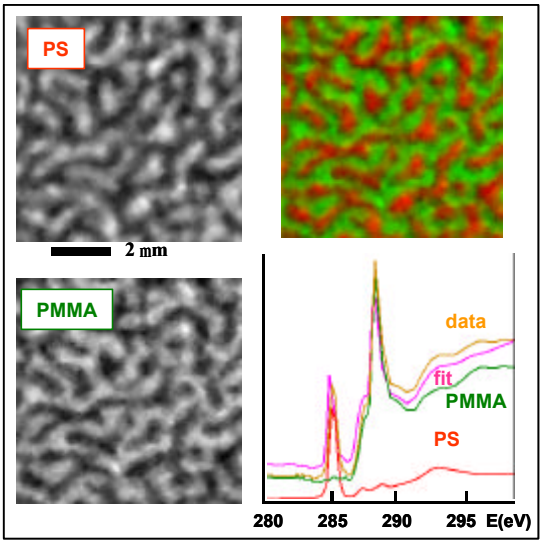

Fig. 4 PS and PMMA component maps, and color composite derived from image sequence of as-made 20:80 PS:PMMA blend, using low dose protocol (3s dwell, chopper=16, few points). Lower right shows the results of a curve fit to the spectrum of pixels in strong PMMA regions. (Jun-01).

SUMMARY: Relative dose - damage relationships for PMMA were measured in PEEM-2 to define an acceptable regime [5]. Similar calibration measurements are required prior to study of other radiation sensitive samples. Self-assembled monolayer and micro-contact printed systems involving fluorocarbons are particularly challenging due to their very small thickness (< 5nm) and extreme radiation sensitivity. An even more rigorous application of the methods outlined in this report is required for successful studies of such materials.

1. C. Morin et al, *J. Electron Spectrosc* 121 (2001) 203-224
2. G. E. Mitchell, et al. 1999 ALS Compendium (2000)
3. C. Morin, A.P. Hitchcock, H. Ikeura-Sekiguchi, A. Doran and A. Scholl, PEEM-2 manual (2001).
4. T. Coffey, S.G. Urquhart and H. Ade, *J. Electron Spectroscopy* 122 (2002) 65.
5. C. Morin, A.P. Hitchcock, et al in preparation.

Supported by NSERC (Canada) and Canada Research Chair program. ALS is supported by U.S. DoE (DE-FG02-89ER60858). Data analysis done with **aXis2000**, an IDL widget available at http://unicorn.mcmaster.ca/aXis2000.html

Principal investigator: *Adam Hitchcock*, McMaster, **aph@mcmaster.ca**. Ph: 905 525-9140

Polarization-dependent soft-x-ray absorption of highly oriented ZnO microrod-array

J.-H. Guo[1], L. Vayssieres[2], C. Persson[2], R. Ahuja[2], B. Johansson[2], and J. Nordgren[2]
[1]Advanced Light Source, Lawrence Berkeley National Laboratory, Berkeley, CA 94720
[2]Department of Physics, Uppsala University, Box 530, S-75121 Uppsala, Sweden

Zinc oxide represents an important basic material (II-VI semiconductor) due to its low cost, wide bandgap as well as its electrical, optoelectronic and luminescent properties. ZnO is of importance for fundamental research as well as relevant for various fields of industrial and high technological applications. Recently, a low threshold lasing action has been observed at room temperature in highly oriented ZnO nanorod arrays. From a fundamental point of view, it is crucial to probe and understand the electronic structure of such novel materials to tailor their physical properties as well as developing novel and improved devices. A novel approach to materials chemistry has been developed which contributed to the fabrication of purpose-built nano/microparticulate thin films from aqueous solution[1]. Such well-defined and well-ordered materials should contribute to reach required enhanced fundamental knowledge of the relation between structure and physical properties.

Here we report a polarization-dependent x-ray absorption spectroscopy (XAS) study performed at synchrotron radiation facility on highly oriented ZnO microrods. The experiments were performed on BL7.0.1 at the ALS[2]. The x-ray absorption spectra were measured by recording the total electron yield while scanning the photon energy over the O *1s*-edge region at a resolution of 0.2 eV. The XAS experiments were carried out on two different (isotropic and anisotropic) homogeneous and crystalline zincite ZnO (wurtzite) thin film samples, i.e. ZnO spheres, which consist of monodisperse spherical particles of 150 nm in diameter, and ZnO microrods consisting of monodisperse, anisotropic and highly oriented crystallites grown along the c-axis and perpendicular to a transparent conducting glass substrate (F-SnO2)\cite{Vayssieres01a}. The microrods of 10 μm in length and 1.5 μm in width are oriented normal to the substrate surface.

The polarization-dependent x-ray absorption measurements are shown in Figure 1. The variations in the spectral shape continue up to 30 eV above the absorption threshold. The resolved absorption features are indicated as a_1-a_8. Prior to a_1, no polarization-dependence is observed in x-ray absorption spectra for either sample. However at higher photon energies, strong anisotropic effects are observed for the ZnO microrods (bottom spectra). Measuring at grazing incidence geometry, i.e. incidence angle $\theta = 10$ degrees, where the absorption features a_3, a_5, and a_8 are stronger, the excitation to the state along the *c*-axis of the wurtzite structure is enhanced. At normal incidence geometry, i.e. $\theta = 90$ degrees, where the absorption features a_2, a_4, and a_7 are stronger, the excitation to the in-plane state is enhanced. No significant change is observed for the isotropic samples of ZnO consisting of spherical particles as a function of the polarization angle. However, all the absorption features are averaged out and observed in the

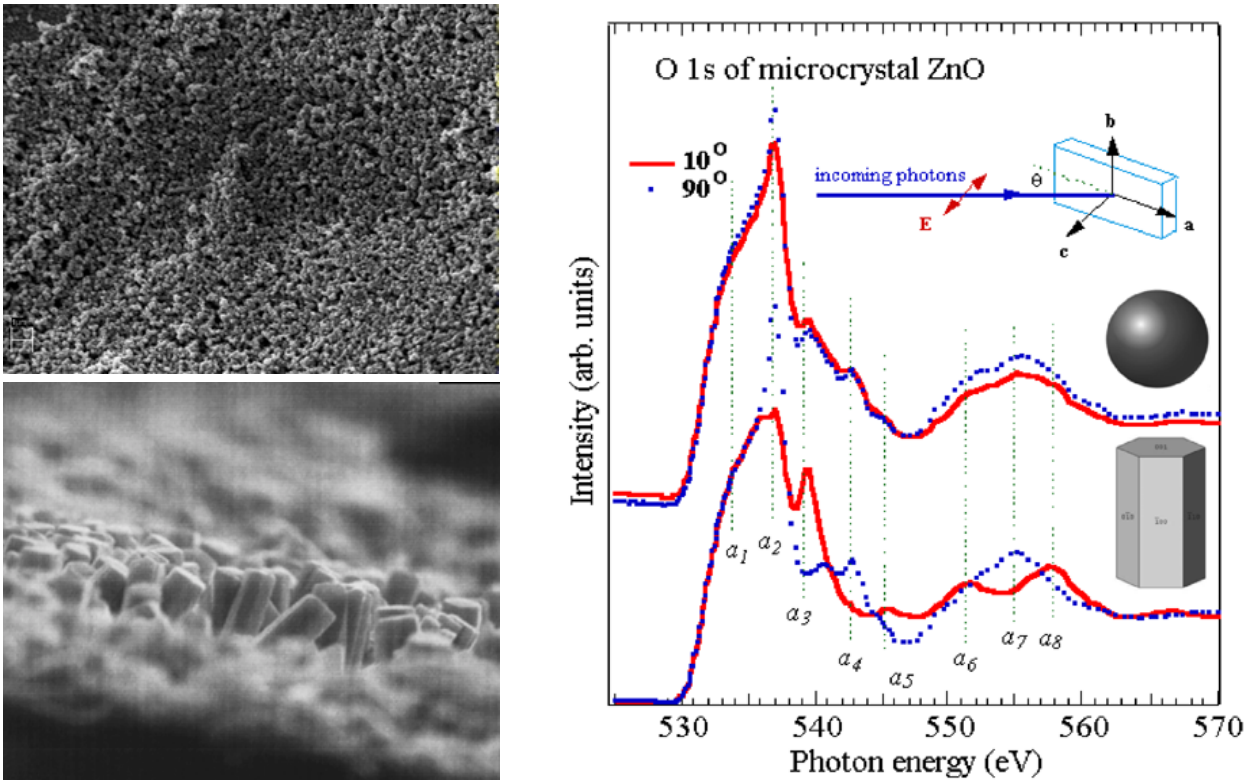

Fig. 1. Polarization-dependent x-ray absorption measurements.

XAS spectra measured with either geometrical detection. The experimental findings suggest a strong correlation between the electronic structure and the geometrical structure of the crystalline ZnO arrays. Such results demonstrate that designing materials with the appropriate morphology and orientation, i.*e purpose-built* materials, enables to reach better fundamental understanding of nano/microscale materials and their physical properties. Probing the orbital symmetry of oxygen and resolving its contribution to the conduction band of this important large band-gap II-VI semiconductor is of crucial importance for the understanding of its optoelectronic properties.

References:

1. L. Vayssieres, A. Hagfeldt and S. E. Lindquist, Pure Appl. Chem. **72**, 47 (2000).
2. T. Warwick, P. Heimann, D. Mossessian, W. McKinney and H. Padmore, Rev. Sci. Instrum. **66**, 2037 (1995).

This work was supported by the Swedish Natural Science Research Council (NFR), Council for Engineering Sciences (TFR), and the Göran Gustafsson Foundation for Research in Natural Science and Medicine (GGS). Department of Energy Materials Sciences Division Contract DE-AC03-76SF00098.

Principal investigator: Jinghua Guo, Advanced Light Source, LBNL. E-mail: jguo@lbl.gov.
Telephone: 510-495-2230.

Quantum confinement observed in α-Fe_2O_3 nanorod-array

J.-H. Guo[1], L. Vayssieres[2], C. Såthe[2], S. M. Butorin[2], and J. Nordgren[2]
[1]Advanced Light Source, Lawrence Berkeley National Laboratory, Berkeley, CA 94720
[2]Department of Physics, Uppsala University, Box 530, S-75121 Uppsala, Sweden

Resonant inelastic x-ray scattering (RIXS) has been applied to the studies of *dd* excitations in MnO and $SrCuO_2Cl_2$ [1,2]. The lowest-lying electronic excitations can be studied most directly by charge neutral spectroscopies, such as electron energy-loss spectroscopy (EELS) and optical absorption. The dd excitations in transition metal compounds are dipole forbidden and therefore very faint in optical spectroscopy.

α-Fe_2O_3 is an antiferromagnetic charge transfer insulator with a bandgap of 2.1 eV. Hematite crystallises in the trigonal system, rhombohedral R-3c group. The crystal structure is the corundum type (Al_2O_3) and can be described as a hexagonal close packed layering of oxygen with 6-fold co-ordinated iron ions yielding to face and edge-sharing octahedra. In an octahedral symmetry, a d^5-configuration is found to have well-separated dd-excitations. Optical absorption spectroscopy of α-Fe_2O_3 has revealed many transitions ranging from infrared to ultraviolet.

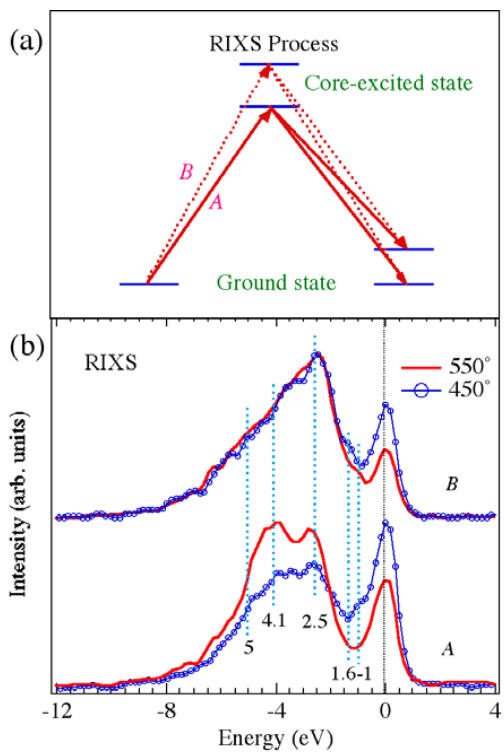

Using the RIXS process, we probed specifically the *dd* excitations in α-Fe_2O_3 by transition sequence $2p^63d^5 \rightarrow 2p^53d^6 \rightarrow 2p^63d^5$. These *dd* transitions become fully allowed, and their intensity can be more easily calculated than that in optical spectroscopy and EELS.

The experiments were performed at beamline 7.0.1 [5] at Advanced Light Source, Lawrence Berkeley National Laboratory. The photon energy resolution was set to 0.2 eV for x-ray absorption spectroscopy (XAS) measurement. The resonant x-ray Raman scattering was measured using a grazing-incidence grating spectrometer [6]. The resolution of both monochromator and fluorescence spectrometer in RIXS measurement was set to 0.5 eV.

The measurements were done on synthetic α-Fe_2O_3 nanorods grown by Controlled Aqueous Chemical Growth [7]. The samples investigated in this letter are thin films, which consist of 3D crystalline array of hematite nanorods bundles of 50 nm in diameter and 500 nm in length perpendicularly oriented onto the substrate. Each bundle was found to consist of self-assembled nanorod of 3-5 nm in diameter. The samples were prepared by

heteronucleation growth and thermodynamic stabilization of akaganeite (β-FeOOH) in solution at 90˚C onto the substrate and subsequently heated in air to 550˚C to allow the crystal phase transition to hematite (α-Fe_2O_3) as confirmed by XRD.

In the resonant inelastic x-ray scattering process, final states probed via such a channel, which are related to eigenvalues of the ground state Hamiltonian. The core-hole lifetime is not a limit on the resolution in this spectroscopy [2]. According to the many-body picture, an energy of a photon, scattered on a certain low-energy excitation, should change by the same amount as a change in an excitation energy of the incident beam (see the decay route of core-excitation *B* versus that of *A* in Fig. 1a). Thus, the RIXS features have constant energy losses and follow the elastic peak.

The RIXS spectra at the Fe *L*-edge of α-Fe_2O_3 nanorods were recorded and shown in Fig.1. A few energy-loss features are clearly resolved. The low energy excitations, such as the strong dd and charge-transfer excitations, are identified in the region from 1 to 5 eV. The 1-eV and 1.6-eV energy-loss features originate from multiple excitation transitions. The 2.5-eV excitation corresponds to the bandgap transition, which is significantly larger than the 2.1-eV-bandgap of single-crystal hematite.

References:

1. S. M. Butorin, J.-H. Guo, M. Magnuson, P. Kuiper, and J. Nordgren, Phys. Rev. B **54**, 4405 (1996).
2. P. Kuiper, J.-H. Guo, C. Såthe, L.-C. Duda, J. Nordgren, J. J. M. Pothuizen, F. M. F. de Groot, and G. A. Sawatzky, Phys. Rev. Lett. **80**, 5204 (1998).
3. L. A. Marusak, R. Messier, and W. B. White, J. Phys. Chem. Solids **41**, 981 (1980).
4. L.-C. Duda, J. Nordgren, G. Dräger, S. Bocharov, Th. Kirchner, J. Electr. Spectros. and Related Phenom. **110-111**, 275 (2000).
5. T. Warwick, P. Heimann, D. Mossessian, W. McKinney and H. Padmore, Rev. Sci. Instrum. **66**, 2037 (1995).
6. J. Nordgren, G. Bray, S. Cramm, R. Nyholm, J. E. Rubensson, and N. Wassdahl, Rev. Sci. Instr. **60**, 1690 (1989).
7. L. Vayssieres, H. Beermann, S.-E. Lindquist, and A. Hagfeldt, Chem. Mater. (in press, 2000).

This work was supported by the Swedish Natural Science Research Council (NFR), Council for Engineering Sciences (TFR), and the Göran Gustafsson Foundation for Research in Natural Science and Medicine (GGS). Department of Energy Materials Sciences Division Contract DE-AC03-76SF00098.

Principal investigator: Jinghua Guo, Advanced Light Source, LBNL. E-mail: jguo@lbl.gov. Telephone: 510-495-2230.

Recent achievements with magnetic soft X-ray microscopy at XM-1

P. Fischer[1], D. Goll[1], T. Eimüller[1], G. Schütz[1], G. Bayreuther[2], T. Ono[3], G. Denbeaux[4], W. Bates[4], E. Anderson[4]

[1]Max-Planck-Institute for Metals Research, Heisenbergstr. 1, 70569 Stuttgart, Germany
[2]Univ. Regensburg, 93040 Regensburg, Germany
[3]Dept. of Electronics and Materials Physics, Graduate School of Engineering Science, Osaka University, Toyonaka, Osaka 560-8531, Japan
[4]CXRO, Cyclotron Road, Berkeley, CA 94720, USA

INTRODUCTION

Studies of magnetic domain structures in systems of low dimensionality are a major issue both from a fundamental physics point of view and in a technologically relevant context. The systems of interest are thin single or stacked multicomponent multilayered magnetic films and are often laterally patterned micro- and nanostructures.Though a large number of imaging techniques is established the outstanding challenge they have to meet, is a layer-resolved (e.g. via chemical sensitivity) spatio-temporal recording of the switching behavior of the magnetic domain structure as this determines largely the technological functionality. Supported by intensive micromagnetic simulations a comprehensive fundamental understanding and a subsequent potential design of the magnetic domain structures is essential.

X-ray magnetic circular dichroism (X-MCD) yields at element-specific spin-orbit coupled (e.g. $L_{3,2}$ and $M_{5,4}$ absorption edges large values up to 50%. In combination with soft X-ray transmission microscopy this serves as huge magnetic contrast mechanism to image magnetic domain structures at a resolution down to 25nm provided by Fresnel zone plate optics (magnetic soft X-ray transmission microscopy (M-TXM)) [1,2]. A description of the technique is found elsewhere [3]. Here we report the recent achievements by selected examples taken at the XM-1 beamline at the ALS/Berkeley CA.

RESULTS

In Fig. 1 the domain pattern of an amorphous 59nm thin $Gd_{25}Fe_{75}$ film with a pronounced perpendicular anisotropy is shown. The images have been taken at the Fe L_3 (a) and the Gd M_5 (b) edge thus probing the local magnetization of Fe and Gd, resp., in an element-specific manner. Though at these two edges the spin-orbit coupling is both parallel the observed reversal of magnetic contrast reflects the antiparallel 3d-4f coupling and proofs the magnetic character of the structures.

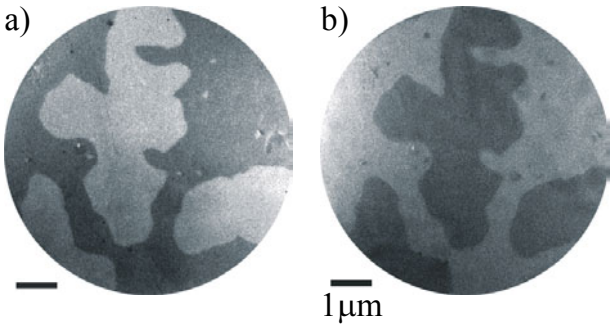

Figure 1 Domain structure of a $Gd_{25}Fe_{75}$ film taken at the Fe L_3 (a) and the Gd M_5 (b) edge.

The magnetization switching can be addressed by recording the domains within complete hysteresis loops. In Fig. 2 a (0.4nmFe/0.4nmGd)x75 multilayered system with lithographically

written line elements with a width of 300nm emerging from a continuous film were studied at saturation (a) and at an applied magnetic field perpendicular to the films surface of 4kOe (b). The maze pattern observed in the continuous film starts penetrating from the left side of the image into the GdFe line structures as a straight line domain. A corresponding white line domains emerges from the right. If the sense of rotation from up to down does not fit for both domains, the melting of these two domains is blocked until at a higher magnetic field finally they are forced to form one single line. As can be seen in the third line from the bottom this is not always the case.

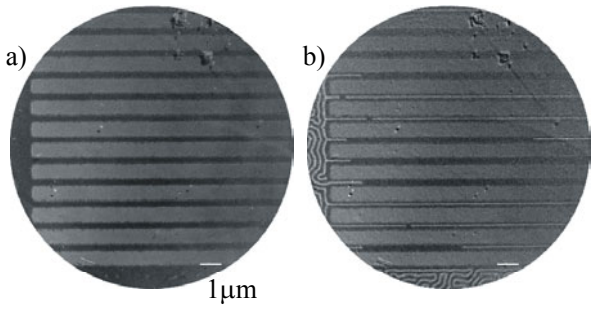

Figure 2 Domain structure in a lithographically edged line pattern (width 300nm) of a multilayered 75x(0.4nm Fe/ 0.4nm Gd) system. a) saturated state, b) domain structure at 0.4kOe.

As the dichroic contrast is given by the projection of the magnetization onto the photon propagation direction both in-plane and out-of-plane systems can be imaged. Amorphous Terfenol-D ($Fe_{66.5}Tb_{9.5}Dy_{24.0}$/2at%Zr) layers exhibit an anisotropy perpendicular to the film plane as they are far from thermodynamically equilibrium.

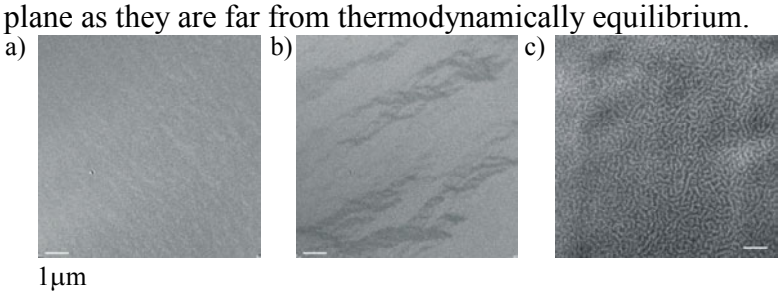

Figure 3 Magnetic domains in Terfenol-D recorded at the Fe L_3 edge in-plane (a,b) and out-of-plane (c).

However, thermal treatment at elevated temperatures (about 500-600K) forces the anisotropy into the film plane. In Fig. 3a) and b) the results obtained with a 70nm thin sample thermally treated at 500K are shown. A typical in-plane domain pattern can be observed if the magnetic field applied along the sample´surface and horizontal in the paper plane is increased from 0 Oe (a) to 200 Oe (b). The corresponding domains for the non-tempered (out-of-plane) system are shown in (c).

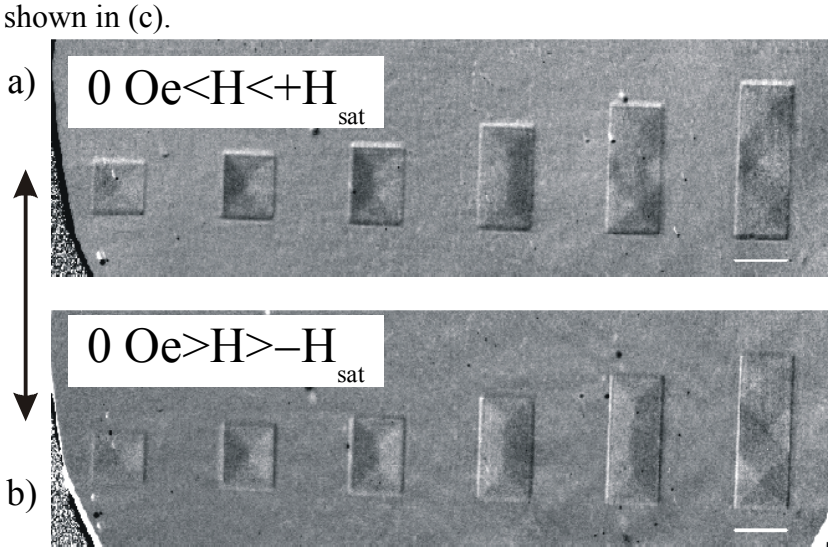

Figure 4 Variation of the domain patterns with size in 50nm thick Permalloy ($Fe_{20}Ni_{80}$) nanostructures. Field direction along the vertical direction (see arrow). The bar is 1μm.The bar is 1μm.

Results of the magnetic domain structure recorded at the Ni L_3 edge within varying external magnetic fields in 50nm thin PY (Permalloy $Fe_{20}Ni_{80}$) patterned elements are shown in Fig. 4. The variation of the domain pattern with varying aspect ratio (width to height) between 1 and 3 is clearly visible. In Fig. 1a) and b) the field direction was along the fixed width of 1µm. Up to an aspect ratio of 1.5 a single closure domain pattern appears, while a more complex configuraton (cross tie wall) emerges for larger aspect ratios.

OUTLOOK

An outlook to the potentials of M-TXM is time dependent imaging where the inherent pulsed time structure of the synchrotron light in the sub-nanosecond regime will be used to study spin dynamics.

ACKNOWLEDGMENTS

We like to thank T. Okuno and T. Shinjo (U Kyoto/Japan) for help with the preparation of samples.

REFERENCES

1. P. Fischer, T. Eimüller, G. Schütz, G. Denbeaux, A. Lucero, L. Johnson, D. Attwood, S. Tsunashima, M. Kumazawa, N. Takagi, M. Köhler, and G. Bayreuther, Rev. Sci. Instr. **72(5)** (2001) 2322-24
2. G. Denbeaux, E. Anderson, W. Chao, T. Eimüller, L. Johnson, M. Köhler, C. Larabell, M. Legros, P. Fischer, A. Pearson, G. Schütz, D. Yager and D. Attwood, Nucl. Instr. And Methods in Phys. Res. A **467-468** (2001) 841-844
3. P. Fischer, T. Eimüller, G. Schütz, M. Köhler, G. Bayreuther, G. Denbeaux, D. Attwood, J. Appl. Phys. **89(11)** (2001) 7159-7161
4. G. Denbeaux, P. Fischer, G. Kusinski, M. LeGros, A. Pearson, D. Attwood, IEEE Trans on Magn. **37** (2001) 2764
5. T. Eimüller, M. Scholz, P. Guttmann, P. Fischer, M. Köhler, G. Bayreuther, G. Schmahl, G. Schütz, J. Appl. Phys. **89** (2001) 7162
6. P. Fischer, T. Eimüller, S. Glück, G. Schütz, S. Tsunashima, M. Kumazawa, N. Takagi, G. Denbeaux and D. Attwood, J. Magn. Soc. of Japan **25**, 186-191 (2001)
7. T. Eimüller, P. Fischer, M. Köhler, M. Scholz, P. Guttmann, G. Denbeaux, S. Glück, G. Bayreuther, G. Schmahl, D. Attwood, G. Schütz, Appl. Phys. A **73** (2001) 697-701
8. T. Eimüller, M. Scholz, P. Guttmann, P. Fischer, M. Köhler, G. Bayreuther, G. Schmahl, G. Schütz, J. Appl. Phys. (2001) submitted
9. P. Fischer, T. Eimüller, G. Schütz und G. Denbeaux, J. Structural Chemistry (2001), submitted

This work was supported by the German Science Foundation, the Volkswagen foundation and the Center for X-ray optics, Berkeley, CA.

Principal investigator: Peter Fischer, Max-Planck-Institute for Metals Research, Heisenbergstr. 1, 70569 Stuttgart, Germany, email: peter.fischer@mf.mpg.de, phone: +49 711 689 1811

Resonant X-ray Fluorescence Holography: Three-Dimensional Atomic Imaging in True Color

S. Omori[1,2,#], L. Zhao[1,3], S. Marchesini[1], M. A. Van Hove[1,3,4], and C. S. Fadley[1,3]

[1] Materials Sciences Division, Lawrence Berkeley National Laboratory, Berkeley, California 94720
[2] Institute of Industrial Science, University of Tokyo, Tokyo 153-8505, Japan
[3] Department of Physics, University of California, Davis, California 95616
[4] Advanced Light Source, Lawrence Berkeley National Laboratory, Berkeley, California 94720
[#]Present address: Sony Research, Kawasaki, Japan

X-ray fluorescence holography (XFH) is a relatively new experimental tool for directly determining the local three-dimensional atomic structure around a given type of atom [1-4]. This element-specific method is based on the same concept as photoelectron holography [5], but detects instead fluorescent x-ray photons.

In the first type of XFH to be demonstrated experimentally [1a], one measures the interference between the fluorescent radiation directly emitted by the excited atoms and additional wave components of the same radiation scattered by various near-neighbor atoms. It is thus necessary to measure a given fluorescent intensity as a function of the direction of emission over as large a solid angle as possible. This method, for which the fluorescent atoms inside the sample act as sources and the intensity is measured in the far field, has been termed normal x-ray fluorescence holography (XFH) [2] or more specifically "direct XFH". In parallel with the first direct XFH experiment, Gog et al. [2a] proposed and demonstrated a different approach (termed multiple energy x-ray holography (MEXH) or "inverse XFH") by applying the optical reciprocity principle and exchanging the roles of source and detector. In this case, the fluorescent atoms inside the sample become the detectors for the net field produced by the interference of the incident x-ray beam and the components of this beam that are scattered by near-neighbor atoms. With present detection systems, MEXH is faster, as the incident beam can be very intense (e.g. emitted directly from a beamline monochromator or an undulator harmonic), and one can furthermore in principle detect all of the fluorescence emitted above the sample surface. Here, one is thus measuring the total fluorescence yield of a given atomic transition as a function of the direction of the incident x-ray beam. Being able to measure at multiple energies also results in images with less aberration due to twin-image effects and other non-idealities [2,5,6]. Recent XFH/MEXH studies have demonstrated the ability to image a first-row element in the presence of a transition metal [3], and to study the local atomic environment in a quasicrystal, even though translational periodicity is lacking for such a system [4]. Current experiments are by and large detector-limited as to the speed of data acquisition. In the ALS Compendium of 2000, we have discussed a project that has successfully measured the first MEXH holograms and holographic atomic images at the ALS [7].

Even though XFH and MEXH in their current formulations offer powerful methods to probe the local atomic structure around a given atom, there still remains one deficiency: the techniques may be element-specific for the central fluorescing atom in the structure (a quality they share with extended x-ray absorption fine structure (EXAFS)), but there is no simple way to determine the

near-neighbor atomic identities. Use can be made of the differences in non-resonant x-ray scattering strengths between different atoms (as is done with differences in electron scattering strength in EXAFS), but this is only unambiguous when atomic numbers are relatively far apart, as recently illustrated for the case of O and Ni in NiO [3]. In the present work, we propose a significant improvement to MEXH, resonant x-ray fluorescence holography (RXFH), that should enable the direct discrimination of different atoms in reconstructed images, even for the most difficult cases where atomic numbers of elements involved are very close together. It is in this sense that we can finally speak of atomic images "in true color" [8].

The principle of RXFH is discussed here for the example of a binary compound of AB_3 type with close atomic numbers, specifically $FeNi_3$, for which Z_{Ni} - Z_{Fe} = 2 and the fractional change in atomic number is only ~0.08 [8]. The central fluorescing atom of the reconstructed images is always chosen to be atom *A* (Fe in this case), and the anomalous dispersion associated with an absorption edge for element *B* (Ni in this case) is used to selectively image atoms *B* surrounding the central atom. In the usual implementations of MEXH in which both atoms *A* and *B* are to be equally imaged, the incident x-ray energies *E* are usually chosen in such a way that they are close enough to E^A_{abs}, the absorption edge of element *A*, for the efficient excitation of fluorescent x-rays from *A*, but also far enough from both E^A_{abs} and any edges E^B_{abs} of atom B that the anomalous dispersion terms in the x-ray scattering factors for *A* and *B* are not significant. In RXFH, by contrast, we will choose several *E*'s in the vicinity of an absorption edge E^B_{abs} of element *B*. The basic idea here is thus similar to that of multiple-wavelength anomalous diffraction (MAD) for phase determinations in conventional x-ray diffraction studies, but with the significant difference that there is from the outset no phase uncertainty in MEXH.

Making use of experimentally determined x-ray scattering factors for Fe (non-resonant) and Ni (resonant), as shown in Fig. 1, we have thus theoretically simulated holograms [6b] for a large cluster of atoms representing the $FeNi_3$ lattice as the Fe Kα fluorescence at 6.4 keV is monitored while scanning through the Ni K edge at about 8.3 keV [8]. As a first trial set of data, we have finally obtained MEXH and RXFH images based on the three energies shown in Fig. 2: below, on, and above the Ni K edge. One promising procedure for imaging in RXFH is shown elsewhere [8] to be using two difference holograms for E_1-E_2 and (with reversed sign) E_3-E_2. Fig. 2 shows the $FeNi_3$ crystal structure, together with normal MEXH images and RXFH images from these difference holograms. Fig. 2 makes it clear that the Ni-atom images are strongly suppressed in the RXFH images, thus suggesting this as a new approach in x-ray fluorescence holography for identifying near-neighbor atoms to a given type of fluorescent emitter.

In conclusion, resonant x-ray fluorescence holography should make it possible to obtain additional information on near-neighbor chemical identities that would lead to a much more complete structural characterization of any system, particularly one in which possible compositional disorder on the nm scale is present, and thus to a much broader applicability for nanoscale materials characterization. Future experiments at the ALS will explore this approach experimentally.

REFERENCES

[1] (a) M. Tegze, G. Faigel, Nature 380 (1996) 49; (b) (b) G. Faigel and M. Tegze, *Rep. Prog. Phys.* **62** (1999) 355.

[2] (a) T. Gog, P.M. Len, G. Materlik, D. Bahr, C.S. Fadley, C. Sanchez-Hanke, Phys. Rev. Lett. **76** (1996) 3132; (b) P.M. Len, C.S. Fadley, and G. Materlik, in X-ray and Inner-Shell Processes: 17th International Conference, R.L. Johnson, H. Schmidt-Böcking, and B.F. Sonntag, Eds., AIP Conference Proceedings, No. 389 (AIP, New York, 1997) p. 295.
[3] M. Tegze, G. Faigel, S. Marchesini, M. Belakhovsky, O. Ulrich, Nature 407, (2000) 38.
[4] S. Marchesini, et al., Phys. Rev. Lett. 85, (2000), 4723-6
[5] G.R. Harp, D.K. Saldin, B.P. Tonner, Phys. Rev. Lett. 65 (1990) 1012; plus more recent work at the ALS by P.M. Len et al. Phys. Rev. B **59** (1999) 5857
[6] (a) P.M Len, Ph.D. thesis, University of California at Davis (1997) and (b) simulation and imaging software described at http://electron.lbl.gov/holopack/holopack.html.
[7] S. Marchesini, L.Zhao, L. Fabris, M. W. West, J. Bucher, D. K. Shuh, W. C. Stolte, M. J. Press , A.S. Schlachter, Z. Hussain, and C. S. Fadley, ALS Compendium of Abstracts 2000: http://alspubs.lbl.gov/AbstractManager/uploads/00135.pdf.
[8] S. Omori, L. Zhao, S. Marchesini, M.A. Van Hove, and C.S. Fadley, Phys. Rev. B **65** (2002) 014106.

This work was supported by the U.S. Department of Energy, Office of Science, Office of Basic Energy Sciences, Materials Sciences Division, under Contract No. DE-AC03-76SF00098..

Principal investigator: Stefano Marchesini, Materials Sciences Division, Lawrence Berkeley National Laboratory. Email: marchesini@lbl.gov. Telephone: 510-486-4581.

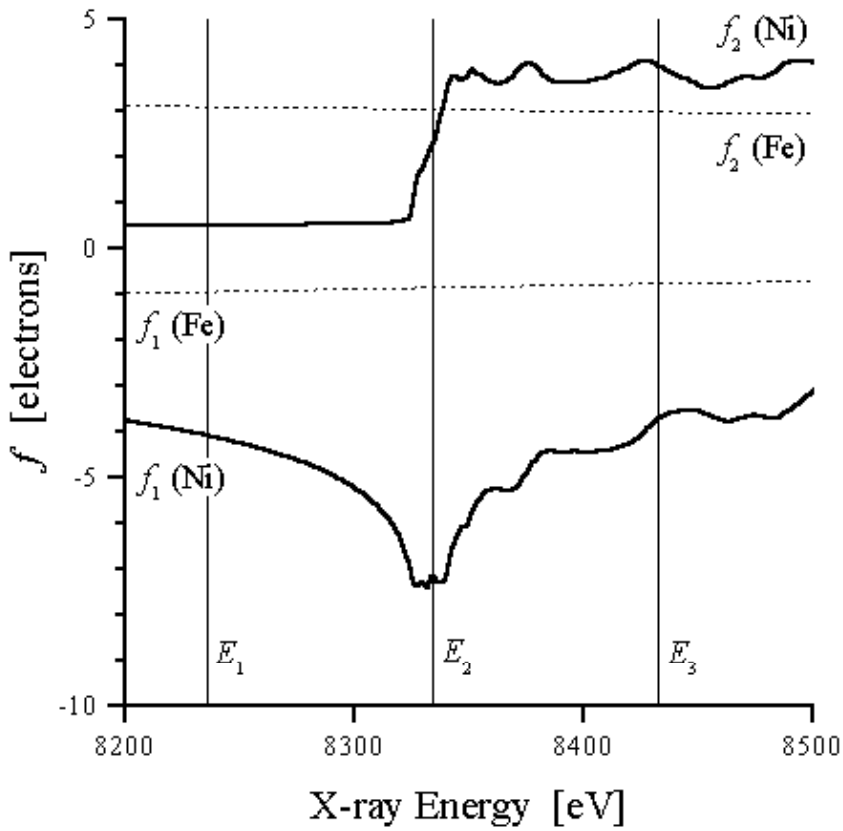

Fig. 1-- The atomic x-ray scattering factors f_1 and f_2 for Fe (dotted lines) and Ni (solid lines) as a function of x-ray energy around the K edge of Ni. The overall scattering factor is given by $f_{Atom} = f_0(\theta) + f_1 - if_2$, with $f_0(\theta)$ the form factor. The three energies used for the simulations of E_1, E_2 and E_3 are indicated by vertical solid lines and correspond to 8235 eV, 8334 eV, and 8433 eV, respectively.

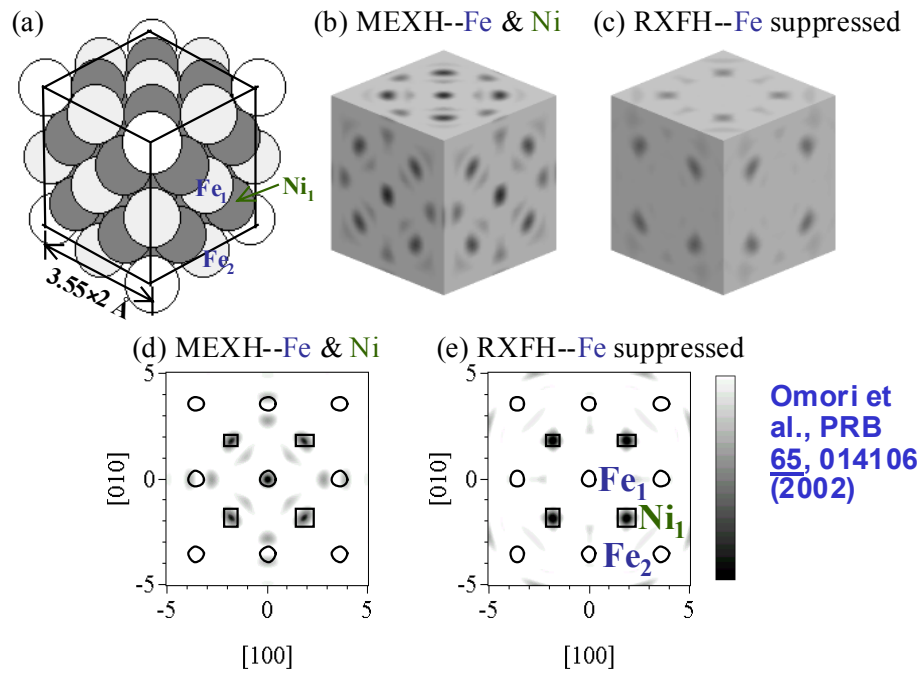

Fig. 2-- Comparison of multi-energy inverse x-ray fluorescence holographic images based on the negative of the real part of images generated using both the standard inversion algorithm (MEXH) and resonant holography (RXFH) based on two difference images (E_1-E_2 and E_3-E_2). These images are based on single-scattering cluster simulations of holograms [6b] at the three energies E_1, E_2 and E_3 for an $FeNi_3$ crystal containing about 10,000 atoms. (a) Near-neighbor atomic model of $FeNi_3$ for comparison to the reconstructed images in (b) and (c) and including 8 unit cells with the lattice constant of 3.55 Å. Fe atoms are lighter gray, and Ni atoms darker gray. The unique types of Fe and Ni atoms observed in (b) are labelled as Fe_1, Fe_2 and Ni_1. (b) Three dimensional reconstructed image from MEXH in cross section along six {001} planes. (c) Corresponding image from RXFH. The fluorescing Fe atom is located at the centers of the cubes in (a), (b) and (c). (d) Enlarged reconstructed image from MEXH in the (001) plane. (e) Corresponding enlarged image from RXFH. The true atomic positions of Fe and Ni atoms are shown as circles and squares, respectively, and certain key atomic positions are also labelled.

Soft X-ray absorption spectroscopy of *single* nanocrystals

F. Nolting[1,2,5], J. Rockenberger[3,4], J. Lüning[2], J. Hu[3,4], and A. P. Alivisatos[3,4]
[1]Advanced Light Source, Ernest Orlando Lawrence Berkeley National Laboratory, Berkeley, CA 94720, USA
[2]Stanford Synchrotron Radiation Laboratory, Stanford, CA 94309, USA
[3]Universtiy of California at Berkeley, Department of Chemistry, Berkeley, CA 94720, USA
[4]Lawerence Berkeley National Laboratory, Materials Science Division, Berkeley, CA 94720, USA
[5]Swiss Light Source, Paul Scherrer Institut, 5232 Villigen PSI, Switzerland

INTRODUCTION

A common limitation in nanostructure research is often the requirement to perform experiments on ensembles of nanoparticles, therefore averaging over inherent distributions with respect to particle size and shape, chemical composition, crystallinity and defect structure. This limitation can be overcome by studying the properties of a single nanostructure individually, which will allow to truly correlate scaling laws of material properties with changes in size. Here, we demonstrate the applicability of spatially resolved Photoemission Electron Microscopy (PEEM) to measure soft x-ray absorption spectra at the Fe $L_{3,2}$ edges of *single* colloidal iron oxide nanocrystals with an average diameter of 10 nm (~ 20,000 iron atoms). The experiment was carried out with the PEEM2 instrument of the ALS [1]. Details of the experiment can be found in [2,3].

EXPERIMENT

Surfactant-capped nanocrystals of γ-Fe_2O_3 (maghemite) were prepared by a slightly modified version of a recently published procedure using hexadecylamine as surfactant [4]. A fraction was isolated by repeated size-selective precipitation using methanol as precipitating agent and the average particle size was determined by TEM to be 10 nm with a standard deviation of 3 nm. Very dilute toluene solutions of this sample were spin-coated onto silicon wafers that were freshly cleaned by etching with HF and washing with deionized H_2O. The particle coverage of the silicon substrate was determined by high-resolution Scanning Electron Microscopy (SEM) at the National Center for Electron Microscopy, Lawrence Berkeley National Laboratory. From the relative positions of the particles in the SEM images (Fig 1A), a mean first nearest neighbor distance of 485 nm was derived. This is sufficiently larger than the spatial resolution of the PEEM microscope in this study. In contrast to our fist study [2,5] using graphite as substrate, we were never able to resolve these spots into smaller aggregates indicating that they, indeed, represent individual nanocrystals. Also, linescans through individual spots show FWHM in the range of 8 – 15 nm in good agreement with the particle size distribution of the sample as determined by TEM.

The PEEM experiments were performed at the bending magnet beamline 7.3.1.1 of the ALS. The best lateral spatial resolution achieved by PEEM to date is about 20 nm, but it depends strongly, in addition to the settings of the instruments, on the topography and conductivity of the sample. In the studies presented here, the spatial resolution was about 150 nm. Fig. 1B shows a chemical contrast image which was obtained by subtracting an image taken at a pre-edge photon energy (700 eV) from the one taken at the iron L_3 edge (707 eV). Hence, the bright spots indicate the presence of iron oxide nanocrystals. The varying brightness of the spots is most likely related to the rather broad size distribution of the iron oxide nanocrystals in the sample with an average diameter and a standard deviation of 10 nm and 3 nm, respectively. In Fig. 1C, the local x-ray absorption spectra of a location appearing bright in Fig 1B (area I) is compared to the one of a dark area (area II). As expected, the spectrum of the bright spot (area I) shows the signature of the Fe L_3 absorption edge

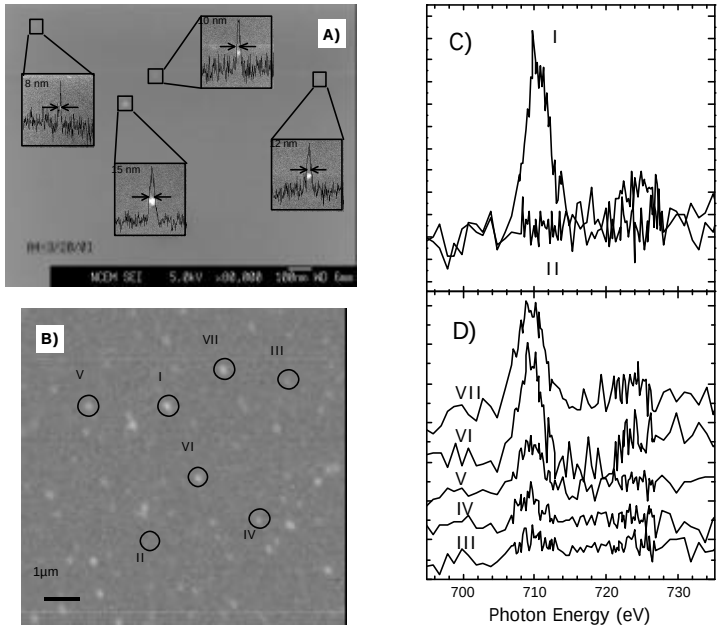

Figure 1: a) High-magnification SEM image of γ-Fe_2O_3 nanocrystals deposited onto Silicon wafer. B) PEEM chemical contrast image. C) Spatially resolved X-ray absorption spectrum recorded in a bright area (I) and a dark area(II). D) Local spectra for different bright spots in b).

at 707 eV, whereas the dark background (area II) shows no detectable structure of the absorption intensity in this energy range. Due to the moderate energy resolution, the multiplet structure of the typical x-ray absorption spectra of Fe^{3+}-ions at the L_3-edge is not resolved. In Fig. 1D, the x-ray absorption spectra of several positions with varying intensities in Fig. 1B (areas III - VII) are compared. Clearly, even in cases with very small intensity in the contrast image in Fig. 1B the Fe L_3 x-ray absorption edge is still discernible from the background whereas the weaker L_2 edge is only barely recognizable. We emphasize that these spectra indeed reflect the x-ray absorption spectra of individual particles with diameters of (10 ± 3) nm with a small chance that some spectra are due to the presence of dimers or trimers of particles (< 13%) [3]. To the best of our knowledge, this represents the first time that soft x-ray absorption spectra of individual nanocrystals at this length scale are reported [6].

This work was supported by the Director, Office of Basic Energy, Division of Chemical Sciences and the Division of Materials Sciences of the U.S. Department of Energy, the Air Force Office of Scientific Research, and the Deutsche Forschungsgemeinschaft.
Principal investigator: Frithjof Nolting. Email: frithjof.nolting@psi.ch. Telephone: +41 56 310 5111.

REFERENCES

[1] S. Anders, *et al.*, Rev. Sci. Instrum. **70**, 3973 (1999).
[2] F. Nolting, J. Lüning, J. Rockenberger, J. Hu, and A. P. Alivisatos, Surf. Rev. Lett. (2002), accepted.
[3] J. Rockenberger, F. Nolting, J. Lüning, J. Hu, A. Paul Alivisatos, J. Chem. Phys. (2002), accepted.
[4] J. Rockenberger, E. C. Scher, and A. P. Alivisatos, J. Am. Chem. Soc. **121,** 11596 (1999).
[5] F. Nolting, J. Rockenberger, J. Lüning, Jiangtao Hu, and A. Paul Alivisatos, ALS Compendium, 2000, LBNL publication, 47838.
[6] Recently, x-ray photoemission spectra of InAs nanocrystals were reported by Heun et al., Phys. Rev. B **2001**, *63*, 125335. They presented averages spectra over all InAs nanocrystals imaged. Also, the InAs nanocrystals with an average diameter and height of 55 nm and 22 nm, respectively, contain significantly more atoms (factor of 40) than the 10 nm γ-Fe_2O_3 nanoparticles investigated here.

Spin-resolved electronic structure studies of ultrathin films of Fe on singular and vicinal GaAs

M. Spangenberg[1], E.A. Seddon[1], E.M.M. McCash[2], T. Shen[3],
S.A. Morton[4], D. Waddill[5] and J. Tobin[4]

[1]CLRC Daresbury Laboratory, Keckwick Lane, Daresbury, Cheshire, UK
[2]Department of Chemistry, University of York, Heslington, York, UK
[3]Joule Physics Laboratory, University of Salford, Salford, Greater Manchester, UK
[4]Lawrence Livermore National Laboratory, 7000 East Ave., Livermore, CA 94550
[5]Department of Physics, University of Missouri-Rolla, Rolla, MO 65409

Recently, there has been considerable interest in the study of spin injection at ferromagnetic semiconductor heterojunctions and ferromagnetic metal – semiconductor contacts[1,2,3,4]. Studies of n-type semiconductors have demonstrated spin-coherent transport over large distances[5] and the persistence of spin coherence over a sizeable time scale[6]. Clearly such investigations have been stimulated by the potential of the development of 'spintronics', electronic devices utilising the information of the electron spin states. To understand and improve the magnetic properties of ultrathin Fe films on GaAs has been the aim of many research groups over recent years. The interest in this system has both technological and fundamental scientific motivations. Technologically, Fe on GaAs may serve to realize spin electronic devices. From a fundamental science point of view, Fe on GaAs serves as a prototype for studies of the interplay between the crystalline structure and morphology of an ultrathin film, its electronic structure and the long range magnetic order it exhibits.

In contrast to the attention given to Fe on variously prepared GaAs substrates, the magnetism of Fe on vicinal GaAs substrates has received scant attention. This in spite of the fact that films grown on vicinal substrates present a number of advantages and opportunities. For example, they are known to exhibit enhanced structural homogeneity, surface diffusion tends to follow well mapped patterns (the quasi-periodicity has been exploited to produce quantum wires) and there is an additional degree of control of the film growth beyond those associated with temperature and substrate surface composition[7].

In a preliminary combined spin-polarized secondary electron spectroscopy, photoelectron spectroscopy and LEED study (carried out on the SRS, Daresbury Laboratory) of the remanent magnetic properties of Fe on singular and vicinal (3° offset) GaAs we have shown both that the various magnetic phases formed are dependant upon the Ga to As surface composition of the substrate and that they evolve in characteristic (but not well understood) ways with Fe overlayer thickness[8]. A remarkable feature in this system, which illustrates the importance of the Fe overlayer/substrate interaction, is the magnetic anisotropy; the easy axis of the Fe films on Ga-terminated substrates is perpendicular to that for As-terminated substrates[9,10].

These measurements were followed up with combined spin-resolved photoemission and magnetic linear dichroism experiments on Fe deposited on vicinal (offcut by 3º and 6º) or singular GaAs substrates on Beamline 7 at the ALS in collaboration with Elaine Seddon of CCLRC Daresbury Laboratory, Dan Waddill of The University of Missouri-Rolla and James Tobin Of Lawrence Livermore National Laboratory. The GaAs(100) substrates were available for film deposition at room temperature after substrate decapping *in-situ* (by thermal annealing),

at the ALS. By mounting both singular and vicinal GaAs substrates on the same sample tile the same growth conditions applied for both films facilitating direct comparison. The surface quality was monitored using LEED. The following data were obtained, high resolution spin-integrated valence bands, the spin-resolved valence bands and their energy dispersion, the film thickness dependence of the spin-resolved valence bands, magnetic linear dichroism data on the Fe3p and Fe2p core levels at a variety of photon energies.

The experiments, which were performed with Dr. Simon Morton and Dr. Jim Tobin in November of 2000 have produced considerable amount of interesting results. The significant differences in the spin-resolved valence bands between *ca.*20 Å thick Fe films on singular and vicinal (3º) GaAs are illustrated in Fig.1. As the terrace width is *ca.*55 Å the spectral differences are not due to step-localized features.

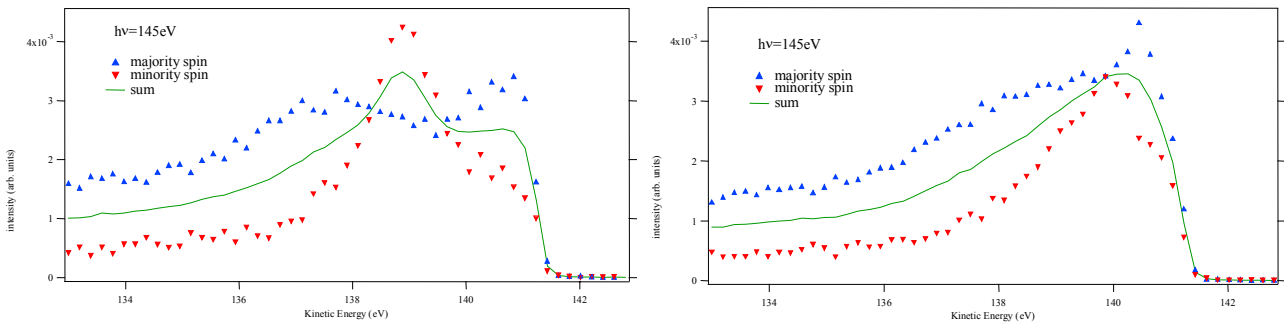

Figure 1
Spin-resolved valence band photoemission results for Fe on singular GaAs (left) and Fe on vicinal (3º) GaAs (right).

Other interesting results include the following. At low film thicknesses, Fe deposited on singular substrates was found to have a lower Curie temperature than Fe on vicinal substrates. Fe deposited on singular substrates reveals a larger energy dispersion of the spin-resolved valence bands than Fe on vicinal substrates. Only marginal differences can be seen between the spin-resolved valence bands of Fe deposited on 3º stepped GaAs substrates and Fe deposited on 6º stepped GaAs substrates. Also, in contrast to the valence band studies, the linear magnetic dichroism results obtained for these samples are very similar.

Further experiments at ALS during oct 2001 enabled us to obtain considerably more interesting results. Whilst the detailed analysis of the results is still underway, Fig.2 shows a large contrast of the valence band spectra of Fe versus incident photon energy between that on a singular and a vicinal substrate. The strong feature on the left in Fig.2 was found to be sensitive to the thickness of the Fe layer and the origin of which is still not yet clear at the present stage.

In summary, the experiments at the ALS have been extremely rewarding. They have answered some questions, clarified our thinking on others and raised yet other questions for which we have no answers at the moment. The run has, however, shown that further access to the ALS is needed to fully understand this fundamental and technologically important system.

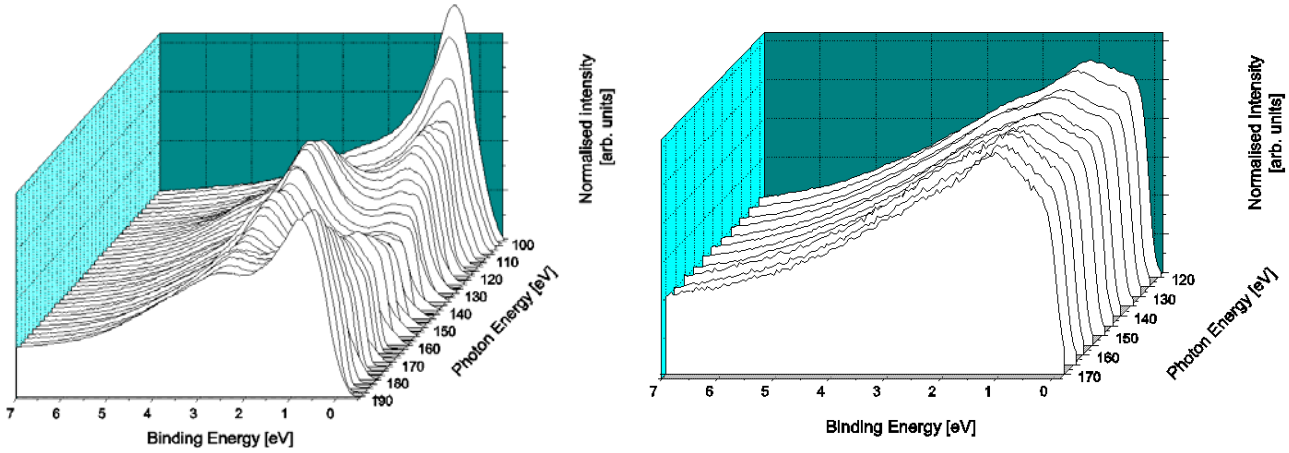

Figure 2.
Valence band spectra of Fe, normalised to the secondary electron tails, versus photon energy for films on singular substrate (left) and on 6 degree vicinal substrate (right).

References:

[1] Malajovich I., Berry J.J., Samarth N. and Awschalom D.D., Nature 411, 770 (2001)
[2] Ohno Y., Young D.K., Beschoten B., Matsukura F., Ohno H. and Awschalom D.D., Nature 402, 790 (1999)
[3] Filip A.T., Hoving B.H., Jedema F.J., van Wees B.J., Dutta B. and Borghs S., Phys. Rev. B 62, 9996 (2000)
[4] Hammar P.R., Bennett B.R., Yang M.Y. and Johnson M., Phys. Rev. Lett. 83, 203 (1999)
[5] Kikkawa J.M. and Awschalom D.D., Nature 397, 139 (1999)
[6] Kikkawa J.M. and Awschalom D.D., Phys. Rev. Lett. 80, 4313 (1998)
[7] Joyce B. A., Neave J. H., Zhang J., Vvedensky D. D., Clarke S., Hugill K.J., Shithara T. and Myers-Beaghton A.K., Semicond. Sci. Technol., **5** 1147 (1990). Kawamura T., Maruta J. and Ishii A., J. Appl. Phys., **39** (7B) 4376 (2000). Gaines J.M., Petroff P.M., Kroemer H., Simes R.J., Geels R.S. and English J.H., J. Vac. Sci. Technol., **B6** 1373 (1998).
[8] Zhang T., Spangenberg M., Greig D., Takahashi N., Shen T-H., Matthew J.A.D., Cornelius S. M., Rendall M. and Seddon, E.A., Appl. Phys. Letters, **78** 961 (2001)
[9] Kneedler E. M., Jonker B. T., Thibado P. M., Wagner R. J., Shanabrook B. V., and Whitman L., J. Phys. Rev. B, **56** 8163 (1997).
[10] Gester M., Daboo C., Hicken R. J., Gray S. J., Ercole A., and Bland J. A. C., J. Appl. Physics **80** 347 (1996).

This work was supported by the Director, Office of Energy Research, Office of Basic Energy Sciences, Materials Science Division, of the U.S. Department of Energy under Contract No. # R5-32633.A02. This work was performed under the auspices of the U.S Department of Energy by Lawrence Livermore National Laboratory under contract no. W-7405-Eng-48. Experiments were carried out at the Spectromicroscopy Facility (Beamline 7.0) at the Advanced Light Source, built and supported by the Office of Basic Energy Science, U.S. Department of Energy.

Principal investigator: E. A. Seddon, CCLRC Daresbury Laboratory, Daresbury, Warrington Cheshire, WA4 4AD, UK, Email: e.a.seddon@dl.ac.uk, Telephone: +44 1925 603245, fax +44 1925 693124

Strain and Stress in a Thin Film $YBa_2Cu_3O_x$ Bicrystal Grain Boundary on $SrTiO_3$ Substrate Studied by X-ray Micro-Diffraction

W.A. Caldwell[1], N. Tamura[1], R.S. Celestre[1], A.A. MacDowell[1], H.A. Padmore[1], and J.R. Patel[1,2]
[1]Advanced Light Source, Ernest Orlando Lawrence Berkeley National Laboratory,
University of California, Berkeley, California 94720, USA
[2]SSRL/SLAC, Stanford University, P.O. Box 43459, Stanford CA 94309, USA

INTRODUCTION

Grain boundaries are important in the electrical transport properties of high-T_c cuprate superconductors. $YBa_2Cu_3O_x$ superconducting devices take advantage of good transport behavior to make wires and use the poor transport (weak link) behavior to make Josephson junction devices [1]. Critical current densities are lower across the grain boundaries by orders of magnitude compared with the values in the bulk of single crystals [2]. The amount of misorientation of neighboring grains is an important parameter in determining the critical current density. In [001] tilt boundaries, one of the simplest grain boundaries, critical current densities drop markedly above 10 degrees [3]. High-resolution electron microscopy has shown that this misorientation angle, which corresponds to the transition from strong to weak intergrain coupling, occurs at the point of overlap of Cu-rich dislocation cores, indicating that the dislocation cores along the grain boundary are responsible for the weak-link behavior [4].

The purpose of this work is to probe the strain/stress of two $YBa_2Cu_3O_x$ bicrystal films near the grain boundary using x-ray microdiffraction in order to visualize the strain/stress fields caused by the dislocation cores at the grain boundary.

EXPERIMENTAL

The samples consist of two $YBa_2Cu_3O_x$ bicrystal samples both with [001] tilt boundaries: one with a 36° tilt (high-angle, weak-link) boundary and the other with a 10° tilt (transition between strong coupling and weak-link) boundary. Both film samples are 260 nm thick and were deposited epitaxially in a controlled (high purity - O_2) environment on $SrTiO_3$ bicrystal substrates and post-growth oxygenated at 420° C for 1 hour prior to removal from the growth chamber.

Oxygen content of our samples were determined from T_c measurements and then used to determine the stress free lattice parameters according to established reference relations [5]. White-beam Laue patterns in reflection mode at beamline 7.3.3 at the Advanced Light Source were taken and automatically indexed using a custom code (X-MAS) developed onsite. The X-ray microdiffraction end station on beamline 7.3.3 has the capability of providing high flux within a beam size of approximately 1 x 1 micron. Its setup has been described elsewhere [6].

RESULTS

Measurements were taken in 1 micron steps to make a raster scan of 30 microns across the bicrystal grain boundary and 10 microns parallel to this boundary for both samples. Additionally, finer scans were made on the 10° sample with 0.5 micron steps of 10 microns by 10 microns and also with 0.25 micron steps of 2 microns by 2 microns. A sample diffraction pattern is shown in Figure 1. The geometrical parameters (sample-detector distance, center channel position and

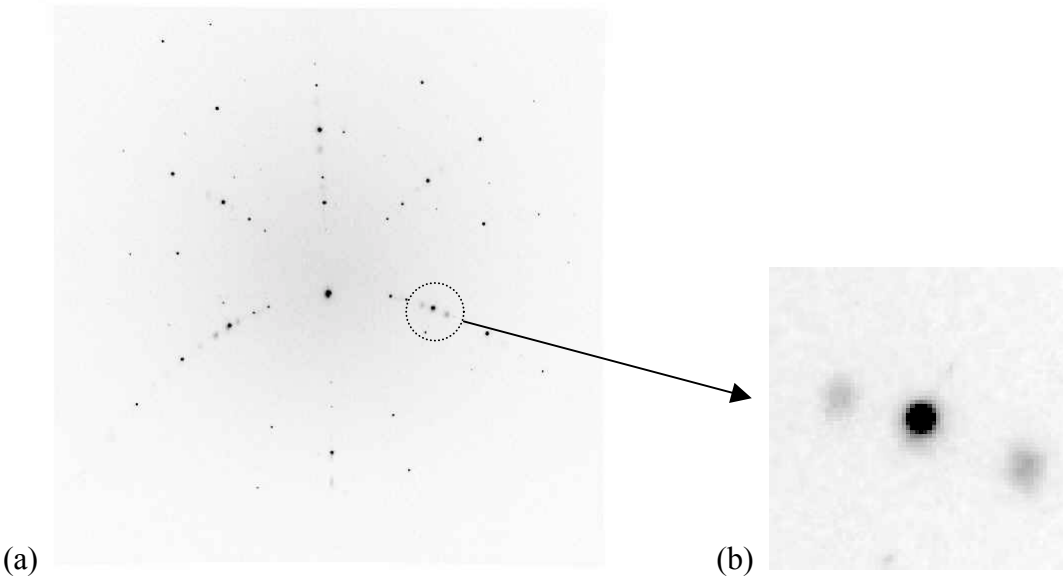

Figure 1. (a) White-beam Laue pattern of $YBa_2Cu_3O_7$ thin film on $SrTiO_3$ bicrystal substrate. (b) The most intense spots are due to the substrate (center of enlarged image). The fainter and more elongated spots are from the film (either side of central spot).

tilts of detector with respect to beam) were determined by using the $SrTiO_3$ substrate as an unstrained reference. T_c measurements of 90.4 K yielded an O_2 content of 7.0, which was then used to calculate the bulk unstrained lattice parameters as: a = 3.8154 Å, b = 3.8888 Å and c = 11.6764 Å.

We found that the strain values in the $YBa_2Cu_3O_7$ film are on the order of 10^{-2} and the effect of the cubic substrate is to make the $YBa_2Cu_3O_7$ structure look tetragonal rather than orthorhombic. The values are consistent with epitaxial strains due to the difference in lattice parameters of the substrate and the film. Due to the large strain values, automated indexation of the diffraction pattern is not straight forward because of the necessity to use a large angular tolerance. We therefore used as an intermediate unstrained reference quadratic values for the $YBa_2Cu_3O_7$ lattice constants and then compare the refined values with the bulk reference. Figures 2 and 3 give the deviatoric strain along the crystallographic unit cell directions, a and b, averaged for the 10 traverses across the grain boundary in the 36° and 10° tilt samples, respectively.

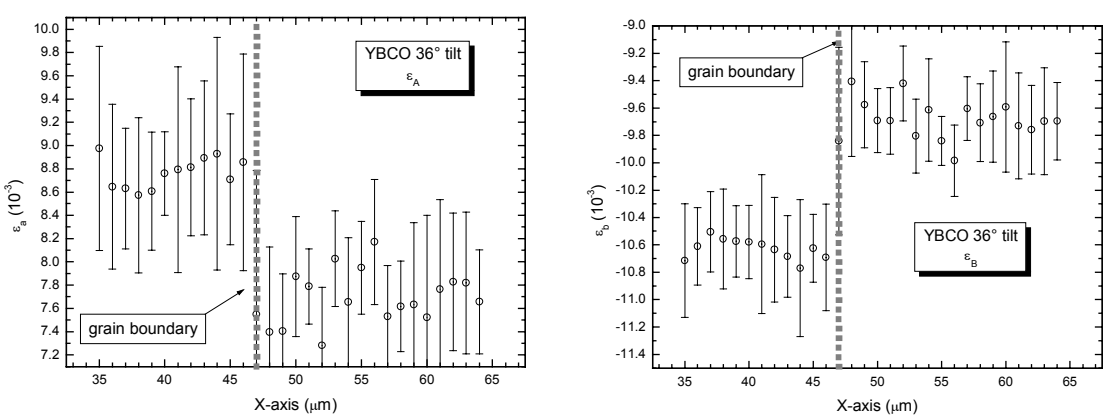

Figure 2. Deviatoric strain measurements along the a-direction (left) and the b-direction (right) of the unit cell averaged over 10 traverses across the grain boundary of the 36° tilt bicrystal.

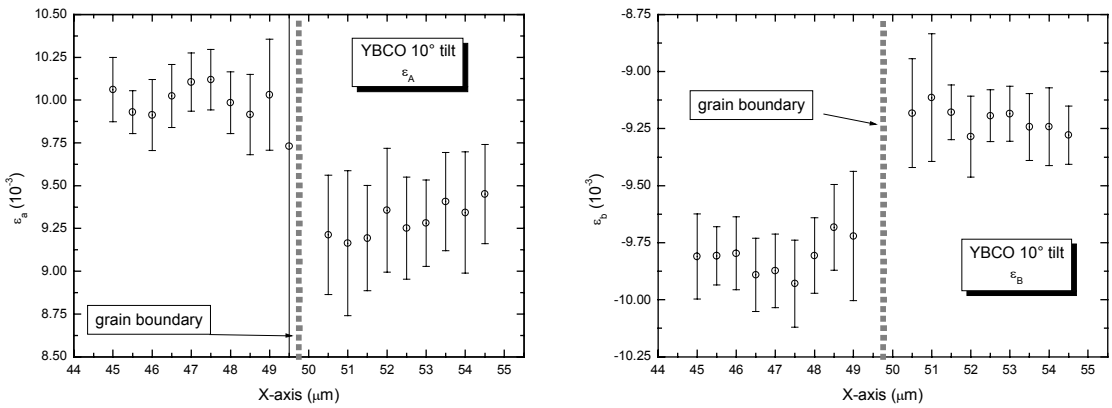

Figure 3. Deviatoric strain measurements along the a-direction (left) and the b-direction (right) of the unit cell averaged over 10 traverses across the grain boundary of the 10° tilt sample.

CONCLUSIONS/DISCUSSION

The deviatoric strain state in the unit cell coordinate system is different on opposing sides of the 36° and 10° bicrystal grain boundary. No strain gradients can be detected within our spatial resolution limit as we approach the grain boundary from either side. Future work will include data collection and analysis at the cryogenic operating conditions of these films.

ACKNOWLEDGMENTS

Thanks to Gertjan Koster and Ted Geballe for providing samples and measuring T_c's.

REFERENCES

1. J. Mannhart and P. Chaudhari, Physics Today **54**, 48 (2001).
2. P. Chaudhari et al., Phys. Rev. Lett. **60**, 1653 (1988).
3. D. Dimos, P. Chaudhari and J. Mannhart, Phys. Rev. B **41**, 4038 (1990).
4. Y. Gao et al., Physica C **174**, 1 (1991).
5. R. G. Munro and H. Chen, J. Am. Ceram. Soc. **79**, 603 (1996).
6. A. A. MacDowell et al., Nucl. Inst. Meth. A **467**, 936 (2001).

This work was supported by the Director, Office of Science, Office of Basic Energy Sciences, Materials Sciences Division, of the US Department of Energy under Contract No. DE-AC03-76SF00098 at Lawrence Berkeley National Laboratory.

Principal investigator: Wendel (Sander) Caldwell, Advanced Light Source, Ernest Orlando Lawrence Berkeley National Laboratory. Email: WACaldwell@lbl.gov. Telephone: 510-495-2233.

X-ray spectromicroscopy of branched polyolefin blends

G. Appel[1], I. Koprinarov[2], G.E. Mitchell[2], A.P. Smith[3] and H. Ade[1]

[1]Department of Physics, North Carolina State University, Raleigh, NC 27695
[2] Analytical Sciences, The Dow Chemical Company, 1897 Building, Midland, MI, 48667
[3]National Institute of Standards and Technology, Polymers Div., Gaithersburg, MD 20899

INTRODUCTION

It is generally difficult to determine the phase diagram of polyolefin blends directly by measuring the composition of phase separated domains. The constituent materials differ only in the amount and/or length of sidechains and provide little spectroscopic differences and limited contrast in traditional miroscopies [1-3]. Indirect methods to determine the phase diagram involve a large number of samples and elaborate contrast enhancement methods. Here, we explore the utility of Near Edge X-ray Absorption Fine Structure (NEXAFS) microscopy to determine polyolefin phase diagrams directly by determining the composition of phases in a limited number of samples. We have used the scanning transmission X-ray microscope (STXM) at beamline 7.0 to investigate thermally annealed blends of an ethylene-butene copolymer (EBC with 3.7 mol % butene) and of an ethylene-octene copolymer (EOC with 3.33 mol % octene). Despite the very similar chemical structure of these copolymers (they differ only in the length of the side chain, i.e. ethyl versus hexyl groups) NEXAFS microscopy can be used to a) directly visualize the morphology without staining or etching, and b) determine the composition of the phases in such blends.

EXPERIMENTAL

0.1 % m/m solutions of EBC and EOC (experimental polymer made with single site catalyst technology) in xylene were mixed in two different ratios (samples A1-4: 33%, samples C1-4 67% EOC). Subsequently, methanol was added to precipitate the polymer. The precipitate was collected by filtering and dried. The samples were vacuum-annealed at 180°C (samples A1, C1), 160°C (samples A2, C2), 140°C (samples A3, C3) and 120°C (samples A4, C4), respectively, quenched to -7°C and cryo-microtomed to about 100-200 nm in thickness.

The data were acquired at beamline 7.0.1. C1s-NEXAFS reference spectra of the pure components were derived from line-spectra (i.e. the same line scan at many photon energies). Image sequences of up to 80 images of small areas (typically 10 μm x 10 μm) as well as small series of large images (typically 6 images, 60 μm x 60 μm) were also recorded.

RESULTS AND DISCUSSION

The C1s-NEXAFS spectra of the two components are shown in Fig. 1. The most noticeable difference between both spectra is found in the 287-288eV energy region. EBC shows two closely spaced peaks (typical for linear polyethylene or polyolefins with few or short side-chains), EOC shows only one broad signal (typical for polyolefins with many or long side-chains). These signals are interpreted as σ^*(C-H) resonances [4]. Their spectral variations primarily reflect different intermolecular distances rather than different degrees of crystallinity. These spectra were used as reference spectra during the "stack fit" procedure [5] to determine the component maps.

Fig. 2 shows typical optical density (OD) images of two of the samples. The domains of the two phases can be clearly distinguished. Because EBC shows a higher absorption coefficient at 288.2eV than EOC (see Fig. 1), regions with high EBC concentration appear bright in Fig. 2b

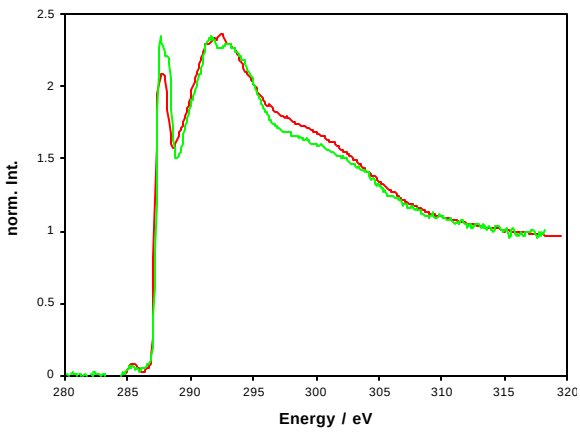

Fig. 1: C1s-NEXAFS reference spectra of the components: Red: ethylene-octene copolymer, green: ethylene-butene copolymer, both normalized to an edge jump of unity between 283eV and 315eV.

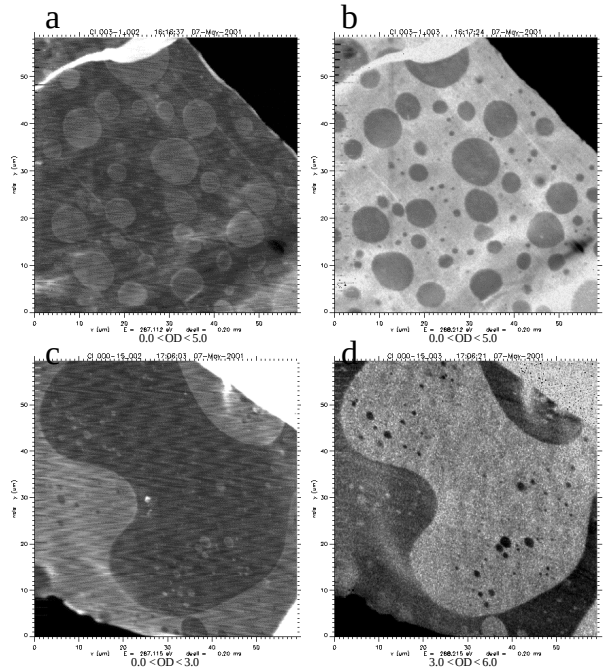

Fig. 2: Typical STXM optical density (OD) images of samples A3 (33% ethylene-octene copolymer): a), b) and C3 (67% ethylene-octene copolymer): c), d). Images a) and c) are taken at 287.1eV. Here domains, which are rich in the ethylene-octene copolymer appear bright. Images b) and d) are taken at 288.2eV and ethylene-butene rich domains appear bright in this case.

and 2d. At 287.1eV the opposite is the case and EOC rich regions appear bright. As expected from the ratio of the components in the mixed solutions, EBC forms the matrix- or majority-phase in sample A3 (a,b) and EOC in sample C3 (c,d).

After the images of an images sequence are aligned to correct for lateral shifts, the spectrum of each pixel in the stack area can be fitted by a linear combination of the reference spectra ($R_{oct}(E)$ and $R_{but}(E)$) and a constant, which is energy-independent (*constant*):

$$OD(E, x, y) = t_{oct}(x,y)*R_{oct}(E) + t_{but}(x,y)*R_{but}(E) + constant(x,y)$$

Thereby matrices of the effective thickness of the components $t_{oct}(x,y)$ and $t_{but}(x,y)$ and of the constant are determined and can be represented by component maps.

From these maps, regions in the matrix and in the minority phase were chosen carefully to not include inclusions of the other phase. Averaging over all pixels of these regions yields the effective thicknesses t. Since the sample contained only the two polymers, the composition Φ_{oct} (here the mass-fraction of EOC) can be calculated:

$$\Phi_{oct} = \frac{t_{oct}}{t_{oct} + t_{but}}$$

Thus, two composition values, one for the matrix and one for the minority phase, are derived for each sample. Fig. 3 shows these results for the different annealing temperatures. If we assume that the thermodynamical equilibrium was reached during the annealing and that the quenching conserved the composition of the melt, this diagram can be interpreted as a phase diagram. Although we presently estimate large errors (10-15%), an upper critical solution temperature behavior and a broad two-phase region is clearly visible.

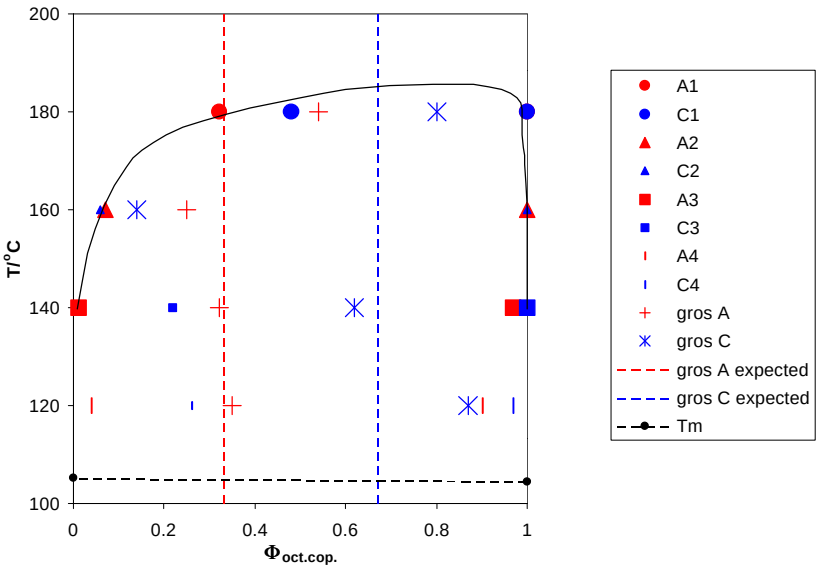

Fig. 3: Proposed phase diagram for the system poly(ethylene-ran-butene) – poly(ethylene-ran-octene). Small symbols were used, if the estimated reliability of the data was low. The gross amounts of the components from area weighted averages of the compositions and the gross amount expected from the preparation are indicated also.

In summary, we used NEXAFS-microscopy to determine the morphology and the composition of a specific polyolefin blend. The differences in the NEXAFS spectra of short- and long-branch copolymers provide sufficient image contrast, especially in the 287-288eV energy region, to image the morphology without further sample preparation (staining, etching). The polymers investigated show phase separation at all annealing temperatures. The matrix phase is always formed by the component that had the higher concentration in the solution and in the case of the EBC rich samples the gross sample composition is close to the solution composition. This indicates an almost quantitative precipitation by methanol. The phase diagram can be determined by quantitative evaluation of image sequences.

REFERENCES

1. M. J. Hill et al., Polymer **41,** 1621 (2000).
2. R. Krishnamoorti et al., J. Chem. Phys. **100,** 3894 (1994).
3. F. M. Mirabella Jr. et al., J. Polymer Sc. B 32, 2187 (1994).
4. A. Schoell A, R. Fink, E. Umbach, S. Urquhart, G.E. Mitchell, H. Ade, in preparation.
5. A. P. Hitchcock, AXIS2000 (Analysis of X-ray microscopy Images and Spectra).

This work was supported by DOE grant DE-FG02-98ER45737.

Principal investigator: Harald Ade, Department of Physics, North Carolina State University, Box 8202, Raleigh, NC 27695, e-mail: harald_ade@ncsu.edu, phone: 919 515 1331